DRAFT VERSION JULY 1, 2019
Preprint typeset using LATEX style emulateapj v. 12/16/11

IMPLICATIONS FROM LATE–TIME X–RAY DETECTIONS OF OPTICALLY SELECTED TIDAL DISRUPTION EVENTS: STATE CHANGES, UNIFICATION, AND DETECTION RATES

P.G. JONKER [1,2], N.C. STONE[3,4,5], A. GENEROZOV[5,6], S. VAN VELZEN[7,8], AND B. METZGER[5]

Draft version July 1, 2019

ABSTRACT

We present *Chandra* X–ray observations of four optically–selected tidal disruption events (TDEs) obtained 4–9 years after their discovery. Three sources were detected with luminosities between 9×10^{40} and 3×10^{42}erg s^{-1}. The spectrum of PTF09axc is consistent with a power law with index of 2.5±0.1, whereas the spectrum of PTF09ge is consistent with the Wien tail of a soft black body best described over the 0.3–7 keV range with a power law of index 3.9±0.5 (the best–fit black body temperature is 0.18 ± 0.02 keV). The power law spectrum of PTF09axc may signal that TDEs transition from an early–time soft state to a late–time low–hard state many years after disruption. The mismatch in Eddington fractions of these sources (≈ 5% for PTF09axc; ≈ 0.2% for PTF09ge) could indicate that, as is the case for X–ray binaries, mass accretion rate is not the sole parameter responsible for TDE state changes. These detections can be used to shed light on the difference between optically selected vs. X–ray selected TDEs. We propose that the time to peak luminosity for optical and X–ray emission may differ substantially in an individual TDE, with X–rays being produced or becoming observable later. This delay can serve to explain the differences in observed properties such as L_{opt}/L_X of optically and X–ray selected TDEs. Using our observations to calibrate simple models for TDE X–ray light curves, we update predictions for the soon–to–be–launched eROSITA instrument, finding an eROSITA TDE detection rate of 3 yr^{-1} to 990 yr^{-1}, a range that depends sensitively on (i) the distribution of black hole spins and (ii) the typical time delay between disruption and peak X-ray brightness. We further predict an asymmetry in the number of retrograde and prograde disks in samples of optically and X–ray selected TDEs, even if the intrinsic number of stars on pro– and retrograde TDE orbits is equal. X–ray selected TDE samples will have a strong bias towards prograde disks (up to 1–2 orders of magnitude if most supermassive black holes spin rapidly, and less so if most spin slowly). On the other hand, in flux–limited samples of optically–selected TDEs, there seems to exist a more modest (typically factor of a few) bias for either retrograde or prograde disks, depending on the underlying optical emission mechanism and regime of loss cone repopulation. These observational biases can contribute to observed differences between optically and X–ray selected TDEs (with optically selected TDEs being fainter in X–rays if the TDE disk is retrograde).

Subject headings: black holes — black hole physics — tidal disruption — active galaxies

1. INTRODUCTION

Stellar tidal disruption is an unavoidable outcome of collisional orbital dynamics in dense stellar systems (Frank & Rees 1976). The stochastic two–body relaxation of orbital parameters leads stars on a random walk through angular momentum space, eventually delivering them to pericenters close to the supermassive black hole (SMBH). Once a star's orbital pericenter falls within the tidal, or Roche, radius of the SMBH, the star will be destroyed upon pericenter passage (Hills 1975; Rees 1988). The resulting tidal disruption events (TDEs) were theoretical curiosities for many years, but have been discovered in increasing numbers over the last two decades. There are now dozens of known TDEs discovered as transient nuclear flares, which have been identified primarily through quasi–thermal emission in soft X-ray (e.g., Bade et al. 1996; Greiner et al. 2000; Komossa et al. 2004; Donato et al. 2014), UV (Gezari et al. 2006, 2009), and optical (van Velzen et al. 2011b; Gezari et al. 2012; Chornock et al. 2014; Arcavi et al. 2014; Holoien et al. 2014, 2016a,b; van Velzen et al. 2019) wavelengths. A minority of TDEs have been observed to launch relativistic jets detectable (via non–thermal hard X–ray and soft γ–ray emission) to cosmological distances (e.g. Bloom et al. 2011; Levan et al. 2011). However, late–time radio followup of thermally–selected TDEs usually returns upper limits (van Velzen et al. 2013; Bower et al. 2013), suggesting that only a minority of TDEs are accompanied by very high luminosity jets (Generozov et al. 2017).

Astrophysical interest in TDEs is manifold. These flares hold great scientific potential as probes of SMBH demographics, as the mass fallback rate onto the black

p.jonker@sron.nl
[1] SRON, Netherlands Institute for Space Research, Sorbonnelaan 2, 3584 CA, Utrecht, The Netherlands
[2] Department of Astrophysics/IMAPP, Radboud University, P.O. Box 9010, 6500 GL, Nijmegen, The Netherlands
[3] Department of Astronomy, University of Maryland, Stadium Drive, College Park, MD 20742-2421, U.S.A.
[4] Racah Institute of Physics, The Hebrew University, Jerusalem, 91904, Israel
[5] Department of Physics, Department of Astronomy, and Columbia Astrophysics Laboratory, Columbia University, New York, NY 10027, USA
[6] JILA, University of Colorado and National Institute of Standards and Technology, 440 UCB, Boulder, CO 80309-0440, USA
[7] Center for Cosmology and Particle Physics, New York University, New York, NY 10003, U.S.A.
[8] Joint Space-Science Institute, University of Maryland, College Park, MD 20742, U.S.A.

hole encodes the mass (Rees 1988; Lodato et al. 2009; Guillochon & Ramirez-Ruiz 2013) of the SMBH. The SMBH spin may be more subtly imprinted into TDE observables (Stone & Loeb 2012; Guillochon & Ramirez-Ruiz 2015; Hayasaki et al. 2016). In the subset of TDEs that launch relativistic jets, radio synchrotron emission produced in the jet forward shock can place tight constraints on circumnuclear gas in distant galactic nuclei (Giannios & Metzger 2011; Berger et al. 2012). More speculatively, these jets could be responsible for the observed flux of ultra–high energy cosmic rays (Farrar & Gruzinov 2009; Farrar & Piran 2014). Exotic TDEs may serve as signposts of unusual SMBH dynamics: truncated light curves are expected in the vicinity of close SMBH binaries (Liu et al. 2009), and off-nuclear TDEs may indicate SMBHs recoiling after anisotropic gravitational wave emission (Stone & Loeb 2011; Jonker et al. 2012). Finally, TDEs may also serve as natural accretion physics laboratories, as the mass fallback feeding the disk declines from super–Eddington levels to a few percent of Eddington over a period of months to years (Shen & Matzner 2014). As TDE accretion rates decline from super–Eddington, to modestly sub–Eddington, to very sub–Eddington levels, their accretion disks might exhibit state changes analogous to those of stellar–mass black holes in X–ray binaries (XRBs; Fender et al. 2004; Komossa et al. 2004).

Early models for TDE light curves and spectra assumed that the highly eccentric debris streams from stellar disruption would quickly circularize into a compact accretion disk (Rees 1988; Cannizzo et al. 1990; Ulmer 1999) that might resemble a scaled–up XRB disk, or the innermost regions of an active galactic nucleus (AGN). A circularized TDE disk would differ from both of these analogues in its radial extent: typically, the tidal radius $R_{\rm t} \lesssim 100 R_{\rm g}$, where $R_{\rm g}$ is the SMBH gravitational radius; a scale much smaller than the typical XRB or AGN disk.

This simple expectation has, however, been strongly challenged. Recent analytic and numerical theory has found that circularization may be very slow if the debris pericenter $R_{\rm p} \gg 10 R_{\rm g}$ (Shiokawa et al. 2015; Dai et al. 2015; Piran et al. 2015) and/or there is strong misalignment between the SMBH spin vector and the debris angular momentum vector (Guillochon & Ramirez-Ruiz 2015; Hayasaki et al. 2016). In tandem, early–time observations have found four properties characteristic of optical/UV-selected TDEs (van Velzen et al. 2011b; Arcavi et al. 2014; Hung et al. 2018):
(i) low blackbody temperatures ($T_{\rm BB} \approx 2\times10^4$ K) with blackbody radii $R_{\rm BB} \sim 10^{2-3} R_{\rm g}$, *(ii)* little cooling ($d\ln(T_{\rm BB})/dt < 0.01$ day^{-1}) over a $\sim$100 day baseline, *(iii)* a steep power–law decay in observed flux $F(t)$ often consistent with $F \propto t^{-5/3}$, and *(iv)* very high optical/UV luminosities, with $L_{\rm BB} \sim 10^{43.5-44.5}$ erg s^{-1} near peak.

All of these properties are inconsistent with the simplest TDE emission model, which assumes emission from radii $\lesssim R_{\rm t} \sim 10 R_{\rm g}$ (Ulmer 1999). In this scenario, the optical/UV emission is far down the Raleigh–Jeans tail of the disk spectral energy distribution (SED), and therefore decays slowly in time, $L_{\rm RJ} \propto T_{\rm BB} \propto t^{-5/12}$ (Lodato & Rossi 2011). The predicted level of optical/UV luminosity is $L_{\rm opt} \sim 10^{41}$ erg s^{-1}, far lower than observed. These discrepancies have motivated multiple theoretical alternatives for the observed optical/UV emission: photon–driven (Strubbe & Quataert 2009) or line–driven (Miller 2015) outflows; emission powered by shocks at debris stream self-intersections (Piran et al. 2015); or thermal reprocessing of accretion power by a layer of gas at large radii (Loeb & Ulmer 1997; Guillochon et al. 2014a).

Conversely, soft X–ray observations of TDEs are more qualitatively consistent with the simple picture of a compact accretion disk. Most X–ray detections of TDEs find very soft spectra, consistent with the Wien tail of (multi–color) black bodies at temperatures $T \lesssim 0.1$ keV (Auchettl et al. 2017), like a scaled–up version of a high-soft state XRB. However, these X-ray spectra are almost always taken in the first one or two years of the flare, when accretion rates are expected to be, at the very least, at a large fraction of the Eddington limit. Notably, many optically selected TDEs go undetected in X–rays (Gezari et al. 2012) and, vice versa, X–ray selected TDEs often lack optical variability. For instance, the TDE XMMSL1 J074008.2−853927 reported by Saxton et al. (2017a) does not show a large enhancement in the optical. Some even show no evidence for enhanced optical emission. For instance, the TDE SDSS J120136.02+300305.5 discovered by Saxton et al. (2012) had an X–ray luminosity of 3×10^{44}erg s^{-1} at discovery while the optical spectrum obtained 12 days after the X–ray discovery shows no spectroscopic features (such as broad emission lines) that are usually associated with TDEs. A recent X–ray discovered source, XMMSL2 J144605.0+685735 (Saxton et al. 2019, in prep.), also shows little or no optical emission above the contribution of the nuclear region of the host galaxy.

So far, we have discussed the state of the art in *early–time* TDE observations, by which we mean observations taken within two years of the peak of the flare. The behavior of TDE disks at late times is relatively under–explored. We note two differences between the early– and late–time phases:

1. The large theoretical uncertainties associated with circularization and disk formation will be less important long after the peak of the mass return rate. A quasi–circular disk is a more reasonable approximation at late times, even if initial circularization was inefficient due to weak apsidal precession (Shiokawa et al. 2015) or misaligned SMBH spin (Guillochon & Ramirez-Ruiz 2015; Hayasaki et al. 2016).

2. The monotonically declining debris fallback rate suggests that at sufficiently late times, TDE disks may pass through the range of sub-Eddington accretion rates that produces a state change in XRB disks (e.g. van Velzen et al. 2011a; Giannios & Metzger 2011; Tchekhovskoy et al. 2014). This analogy suggests that once TDE accretion rates decline below a few percent of Eddington, X–ray emission may exhibit features of the XRB low/hard state, such as a primarily non–thermal, hard power–law spectrum. Such "SMBH state changes" have not yet been seen in TDEs, although there is one suggestive example: X-ray observations of the TDE in NGC 5905 show a transition from a soft to harder spectrum at late times (Komossa & Bade 1999).

The search for late–time TDE X–ray emission is further motivated by the recent *Hubble Space Telescope* discovery of late–time far UV (FUV) emission in six optically–selected TDEs (van Velzen et al. 2018). In all six cases, the late–time FUV luminosities were well above the levels predicted from extrapolating a naive $\propto t^{-5/3}$ power–law. The observed slower rate of decline hints at a transition from fallback–dominated to disk–dominated accretion rates (Cannizzo et al. 1990), and the small fitted black body radii ($R_{\rm BB} \sim 2-5R_{\rm t}$) indicates that if optically thick reprocessing layers once existed, they have since dissipated. It is therefore reasonable to expect that many optically–selected TDEs should, at late times, be emitting relatively unobscured X–rays from their inner disks.

In this paper, we present and analyze *Chandra* observations of four optically–selected TDEs taken at late times, long after the peak of the optical flare has passed. We have observed PTF09axc and PTF09ge 8 years after their discovery, PTF09djl 9 years after its discovery, and ASASSN–14ae 5 years after its discovery. In §2, we present our observations and results, and in §3, we discuss the implications of both detections and non–detections for broader questions in TDE and accretion physics. We adopt $\Omega_m = 0.3$, $\Omega_\Lambda = 0.7$, and $H_0 = 70$ km s^{-1} Mpc^{-1} to convert the redshift of each source to luminosity distances.

2. OBSERVATIONS, ANALYSIS AND RESULTS

We obtained 69.19, 34.15, 9.6, 19.08 ksec long on–source *Chandra* exposures of PTF09axc, PTF09ge, ASASSN–14ae, and PTF09djl, respectively. The first two sources were observed under *Chandra* Guest Observer program 18700591, and the latter two under 20700515. The observation of PTF09axc was split in two parts of 53.66 and 15.53 ksec in length. The observation identification (ID) numbers for the data presented here are 19532 (53.66 ksec) and 20879 (15.53 ksec) for PTF09axc, 19531 for PTF09ge, 21503 for ASASSN–14ae, and 21504 for PTF09djl with observing dates and start times (UTC) of 2017-12-08 at 23:11:32, 2017-12-06 at 18:12:18, 2017-09-28 at 20:19:15, 2018-11-17 at 21:48:37, and 2019-01-06 at 13:08:18, respectively. A log of the observations can be found in Table 1.

In all cases, the source position as derived in the initial optical outburst was covered by the S3 CCD of the ACIS-S detector array (Garmire 1997). For the observations of PTF09axc and PTF09ge, 3 CCDs were operational (besides the S3 CCD, S4 and S2 were operational) and the full CCDs were read out providing a nominal exposure time per frame of 3.1 sec. For the observations of ASASSN–14ae and PTF09djl we chose to use only the S3 CCD. It was operated in sub–array mode where only a quarter of the CCD is read out. This yields an exposure time of 0.8 s per CCD frame.

We reprocessed and analyzed the data using the CIAO 4.10 software developed by the *Chandra* X–ray Center and employing CALDB version 4.8.1. To allow for a thorough rejection of events unrelated to the source such as cosmic ray hits, the data telemetry mode was set to *very faint*. Using the CIAO tool *wavdetect* we have detected an X–ray source in an image constructed from the 0.3–7 keV data. The position of the X-ray source is consistent with the optical position of the TDE in all three cases where we detected a source close to the expected position (see Table 2). No X–ray source was detected at the location of the optical outburst source in the case of PTF09djl.

For the detected sources we calculate the 95% confidence uncertainty on the *Chandra* X–ray position using eq. 12 in Kim et al. (2007) which contain the off–axis angle and the detected number of source counts. All our sources have been detected on–axis and the number of *wavdetect*–detected counts is given in Table 2. This internal positional uncertainty has to be supplemented with the external uncertainty, which includes the uncertainty in the satellite aspect solution, and the knowledge of the geometry and alignment of the spacecraft and focal plane. Evans et al. (2010) found this external correction to be 0.39″, which was subsequently found to be under–estimated by 0.16″ by Rots & Budavári (2011). The total external 95% confidence uncertainty of 0.55″ needs to be added in quadrature to the internal positional uncertainties given in Table 2.

We use the CIAO tool *specextract* to extract a source spectrum for each of the three detected sources separately, using the best known optical coordinates for the sources (see Table 2 for references). We created source and background regions centered on the optical position of the sources. The circular source regions have a radius of 2″. The background regions for PTF09axc and PTF09ge are annular with inner and outer radii of 10″and 30″, respectively. For ASASSN–14ae, the background is drawn from a source–free, circular region on the same CCD (because of the smaller sky area covered due to the employment of a sub–array in the read-out). This circular region has a radius of 30″. We do not rebin the extracted source spectra, although we require each channel to have at least one X-ray photon. We report the 68% confidence regions for fitted parameters unless mentioned otherwise.

We fitted the extracted spectra of each source individually using the HEASOFT XSPEC tool version 12.10.1. We excluded photons detected outside the range 0.3–7 keV, as this energy interval is the best calibrated and most sensitive range for *Chandra*. Throughout the spectral fitting we employ Cash statistics (Cash 1979) unless mentioned otherwise. For each source we fit the background spectrum separately first. A power law is an adequate, first order, description of the background spectrum (see Table 3). When fitting the source spectrum, the background is described using the shape and parameters fixed to those derived from the separate background fit. We scale the normalization of the power law model (that describes the background) on the basis of the ratio between the size of the source region and that of the background region.

2.1. *PTF09axc*

PTF09axc has a redshift of $z = 0.1146$ (d_L = 532.6 Mpc) and is associated with the galaxy SDSS J145313.07+221432.2 (Arcavi et al. 2014). Given the relatively high observed count rate of PTF09axc we investigate if the source spectrum is affected by pile–up by employing the CIAO tool PILEUP_MAP on an image created including all photon energies for both observations of PTF09axc. The count rate per frame in both observations is less than 0.02, implying a pile–up fraction lower than 1%. Therefore, we conclude that pile–up is insignificant for our observations of PTF09axc and by

TABLE 1
A log of the *Chandra* late–time X–ray observations of four optically selected tidal disruption events. The time since the discovery of the optical transient is denoted with Δt (delay).

Source	Observing date MJD (UTC)	Observation ID	Duration (kilo seconds)	Delay (Δt; yr)
PTF09axc	58095.966	19532	53.66	8.5
PTF09axc	58093.759	20879	15.53	8.5
PTF09ge	58024.847	19531	34.15	8.4
ASASSN–14ae	58439.909	21503	9.6	4.8
PTF09djl	58489.547	21504	19.08	9.5

TABLE 2
World Coordinate System information of our sample.

Source	Optical position	*Chandra* X–ray position	95% conf. internal uncert. [″]	Total 95% conf. uncert. [″]	Offset [″]	Source counts	Ref. †
PTF09axc	14:53:13.06 +22:14:32.2	14:53:13.08 +22:14:32.169	0.11	0.56	0.2	381	[1]
PTF09axc	223.30442 +22.24228	223.30449 +22.24227	0.11	0.56	0.2	381	[1]
PTF09ge	14:57:03.18 +49:36:40.97	14:57:03.18 +49:36:40.865	0.24	0.6	0.1	43	[1]
PTF09ge	224.26325 +49.61138	224.26326 +49.61135	0.24	0.6	0.1	43	[1]
ASASSN–14ae	11:08:40.12 +34:05:52.23	11:08:40.13 +34:05:53.045	0.56	0.78	0.8	8	[3]
ASASSN–14ae	167.16717 +34.09784	167.16719 +34.09807	0.56	0.78	0.8	8	[3]
PTF09djl	16:33:55.94 +30:14:16.3	–	–	–	–	–	[1]
PTF09djl	248.4831 +30.23786	–	–	–	–	–	[1]

† Reference for the optical coordinates of the sources: [1] Arcavi et al. (2014); [3] Holoien et al. (2014)

Note. — Optical and *Chandra* X–ray coordinates of the tidal disruption events in our sample, the offset between the two and the number of X–ray counts detected in the observation between 0.3–7 keV. The nominal external uncertainty on the *Chandra* X–ray coordinates is 0.55″ at 95% confidence. We have chosen to add this in quadrature to the provided internal uncertainty in the fourth column. For PTF09axc we report the values found in Obs ID 19532 as this is the longer of the two, providing significantly more source counts. The coordinates found when using Obs ID 20879 are fully consistent with this.

extension, given that the other sources we observed have a lower count rate per frame, those spectra are not affected by pile–up either.

In the fit we take the attenuating effect of Galactic foreground extinction into account. To model this effect we use the xspec phabs multiplicative model, where we convert the $A_V = 0.098$ for Galactic foreground extinction obtained through NED (Schlafly & Finkbeiner 2011) to an $N_H = 1.8 \times 10^{20}$ cm^{-2} using the relation $N_H = 1.79 A_V \times 10^{21}$ cm^{-2} (Predehl & Schmitt 1995). The value of N_H is kept fixed during the fit. We employ the xspec fit–function pegpwr + phabs × pegpwr. For here and below, we note that in all cases the normalisation of the pegpwr function is equal to the unabsorbed 0.3–7 keV flux.

Fitting the two observations together, the spectrum of PTF09axc is well–fit by a power law with index Γ=2.5±0.1, with an unabsorbed 0.3–7 keV flux of (9.5±0.6)$\times 10^{-14}$erg cm^{-2} s^{-1} translating to a 0.3–7 keV luminosity $L_X = (3.2 \pm 0.2) \times 10^{42}$erg s^{-1}, where in the calculation of the luminosity uncertainty we, here and below, only included the uncertainty in the flux measurement and not that in the distance determination. The observed, absorbed, 0.3–7 keV flux is (8.5±0.5)$\times 10^{-13}$erg cm^{-2} s^{-1}. The C-statistic of the fit was 226.6 for 223 bins and 221 degrees of freedom. Using the goodness command in xspec we obtained that 100% of the realizations yield a lower fit statistic.

For reference, given the observed number of background events extracted in the background region (1720 for obs ID 19532 and 479 in obs ID 20503) one expects that out of the 447 detected counts at the source position (375 and 72 for the two obs IDs, respectively), 11 are due to the background (8.5 and 2.4 for the two obs IDs, respectively).

To check our results, we rebinned the data of obs ID 19532 (the longer of the two observations), requiring that each bin contains at least 30 counts. We subtracted the background and fit the resulting spectrum with a power law attenuated by the foreground Galactic extinction employing Chi–squared statistics. The result is fully consistent with that obtained fitting the unbinned data on both data sets. Given the high number of counts detected, we produced a light curve of the observation with ID 19532 with 1 ksec–long bins to investigate if flares are present: none were found.

2.2. *PTF09ge*

PTF09ge has a redshift of $z = 0.064$ (d_L = 287.4 Mpc) and is associated with the galaxy SDSS J145703.17+493640.9 (Arcavi et al. 2014).

The spectrum of PTF09ge is relatively soft compared to the spectrum of PTF09axc: no photons with energies above 2 keV are detected. We fitted the source spectrum with a redshifted black body including a power law model for the background using Cash statistics. As for PTF09axc our fit–function includes a factor to model the foreground extinction, N_H. For this we use a rounded–off value of 1×10^{20} cm^{-2} given the $A_V = 0.046$ from NED (Schlafly & Finkbeiner 2011). The value of N_H is kept fixed during the fit.

Fitting the source and background together, we use a fit–function of an absorbed, redshifted black body for the source plus a power law for the background (PEGPWR + PHABS × ZASHIFT × BBODYRAD in XSPEC). We find a best-fit value for the black body temperature of 0.18±0.02 keV. The unabsorbed source flux, subtracting the flux due to the background power law in the 0.3–7 keV range is 1.9×10^{-14}erg cm^{-2} s^{-1} giving a 0.3–7 keV luminosity of $L_X = 2\times10^{41}$erg s^{-1}. The absorbed 0.3–7 keV flux is $(1.7^{+0.3}_{-0.5})\times10^{-14}$erg cm^{-2} s^{-1}. The C-statistic of the fit was 34.5 for 29 bins and 27 degrees of freedom. Using the GOODNESS command in XSPEC we obtained that 98% of the realizations yield a lower fit statistic (when all simulations are drawn from the best-fit model). The bolometric source luminosity is 2.7×10^{41}erg s^{-1}.

As the fit shows some notable residuals, it mostly under-predicts the flux at low energies, we also try the simple fit–function used for PTF09axc (PEGPWR + PHABS × PEGPWR in XSPEC). For this power law fit we find a best-fit value for the power law index of 3.9±0.4, and an unabsorbed source flux in the 0.3–7 keV range of $3.9^{+1.2}_{-0.9}\times10^{-14}$erg cm^{-2} s^{-1} giving a 0.3–7 keV luminosity of $L_X = 3.9^{+1.1}_{-1.0}\times10^{41}$erg s^{-1}. The absorbed 0.3–7 keV flux is $(3.5\pm0.9)\times10^{-14}$erg cm^{-2} s^{-1}. The C-statistic of the fit was 25.2 for 29 bins and 27 degrees of freedom. Using the GOODNESS command in XSPEC we obtained that 58% of the realizations yield a lower fit statistic (again when all simulations are drawn from the best-fit model).

2.3. *ASASSN–14ae*

ASASSN–14ae has a redshift of $z = 0.043671$ ($d_L = 193.3$ Mpc) and is associated with the galaxy SDSS J110840.11+340552.2 (Holoien et al. 2014). For foreground extinction, N_H, we use a rounded–off value of 1×10^{20} cm^{-2} given the $A_V = 0.048$ from NED (Schlafly & Finkbeiner 2011). The value of N_H is kept fixed during the fit.

Eight photons are detected at a position consistent with that of the optical source in outburst. Owing to the relative short exposure compared to the other observations we report on in this manuscript, on average only 0.3 background counts would fall in the source extraction region. Given this very low back ground event rate the eight–count detection is highly significant: i.e. it occurs due to chance in approximately one out of 8×10^8 cases. For our spectral analysis of these eight photons we do not correct for this expected background. We fitted for the power law index and normalisation in the fit–function PHABS × PEGPWR in XSPEC. The best–fit power law index is $\Gamma = 3.2\pm1.0$. The unabsorbed 0.3-7 keV flux is $(2^{+2}_{-1})\times10^{-14}$erg cm^{-2} s^{-1}, giving a 0.3–7 keV luminosity of $(9^{+9}_{-5})\times10^{40}$erg s^{-1}. The absorbed 0.3–7 keV flux is $(1.8\pm0.8)\times10^{-14}$erg cm^{-2} s^{-1}. The C-statistic of the fit was 17.6 for 8 bins and 6 degrees of freedom. Using the GOODNESS command we obtained that 96% of the realizations yield a lower fit statistic (again when all simulations are drawn from the best-fit model).

2.4. *PTF09djl*

PTF09djl has a redshift of $z = 0.184$ ($d_L = 893.2$ Mpc) and is associated with the galaxy SDSS J163355.96+301416.6 (Arcavi et al. 2014). For foreground extinction, N_H, we use a rounded–off value of 1×10^{20} cm^{-2} given the $A_V = 0.049$ from NED (Schlafly & Finkbeiner 2011). The value of N_H is kept fixed during the fit.

No X–ray photons with energies between 0.3–7 keV have been detected in a circle with a radius of 1″ centered on the optical outburst position of PTF09djl. We estimate the average background photon rate in 0.3–7 keV by extracting the detected counts in a circular region with a radius of 30″ close to the source where no sources were found when using the WAVDETECT tool with default parameters. 110 background photons are detected in such a region centered on coordinates RA 16:33:52.17 Dec. +30:13:44.9, implying that on average 0.12 background count is expected in a 1″ circular region.

Following Kraft et al. (1991) and Helene (1984), we derive a 95% confidence upper limit on the number of detected source counts in the 0.3–7 keV band of 3. To convert this to a limit on the flux, we divide the upper limit on the detected number of source counts by the on–source time of this observation to obtain an upper limit on the source count rate. Next, we use two models for the spectral shape of the source: a blackbody with a temperature of 180 eV similar to that found for PTF09ge, or a power law with index of 2.5, as was found for PTF09axc. The attenuating effect of the N_H derived above is marginal and therefore ignored. W3PIMMS[9] provides a 95% upper limit to the (absorbed) 0.3–7 keV X–ray flux of $F_X \leq 3\times10^{-15}$ erg cm^{-2} s^{-1} both for the power law model and for the black body model. This yields an upper limit to the source 0.3–7 keV luminosity of $L_X \leq 3\times10^{41}$ erg s^{-1} for both models.

3. DISCUSSION

We observed four optically selected TDEs in X–rays using the *Chandra* satellite. One source, ASASSN–14ae, was observed 4.8 yr after its discovery by Holoien et al. (2014), while the other three sources were observed ≈8–10 yr after their discovery by Arcavi et al. (2014). Three of the four sources were detected; only PTF09djl remains undetected. The X–ray detections of PTF09axc and PTF09ge are especially interesting in conjunction: the X–ray spectrum of PTF09axc is well–fit with a power–law ($\Gamma = 2.5\pm0.1$); conversely, our observations of PTF09ge are well–fit by a blackbody Wien tail that manifests itself in the 0.3–7 keV *Chandra* band as a very soft, $\Gamma = 3.9\pm0.4$ power law. Finally, for ASASSN–14ae, the number of detected X–ray photons is too low for a meaningful spectral fit. Our *Chandra* detections are consistent with the 2014 upper limit of $L_X < 2.3\times10^{42}$ erg s^{-1} for PTF09ge, the 2014 detection of $L_X = 7.1^{+12}_{-3.1}\times10^{42}$ erg s^{-1} for PTF09axc (Arcavi et al. 2014), and the 2014 upper limit of $L_X < 1.3\times10^{41}$ erg s^{-1} for ASASSN–14ae (Holoien et al. 2014).

Our results indicate that optically–selected TDEs may maintain a substantial X–ray luminosity for at least $\sim 5-10$ yr post-peak, long after the optical emission has become undetectable. Notably, several opti-

[9] https://heasarc.gsfc.nasa.gov/cgi-bin/Tools/w3pimms/w3pimms.pl

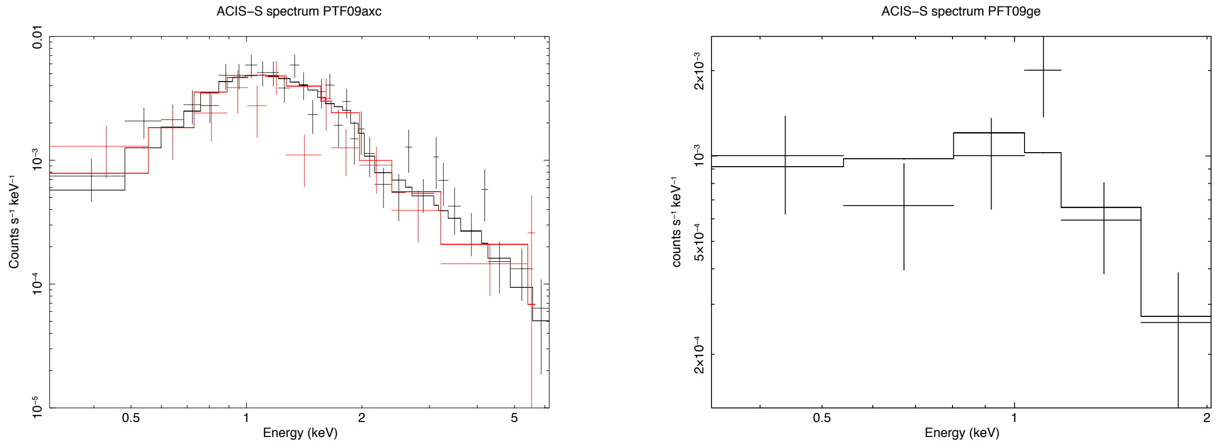

FIG. 1.— *Left panel:* We show the *Chandra* ACIS–S spectrum of PTF09axc fitted with a power law folded through the detector response. The black data points are from observation ID 19532 and the red (/grey) data points are from observation ID 20879. The best–fit power law index is 2.5±0.1. *Right panel:* The *Chandra* ACIS–S spectrum of PTF09ge fitted with a power law. The best–fit power law index is 3.9±0.4, consistent with the slope of the Wien tail of a black body that peaks in the extreme UV.

TABLE 3
X–RAY SPECTRAL FIT–PARAMETERS FOR PTF09AXC, PTF09GE AND ASASSN–14AE. THE NORMALIZATION OF THE BACKGROUND HAS BEEN SCALED DOWN TO MATCH THE SOURCE PHOTON EXTRACTION AREA (THE SCALING FACTOR WAS 200 FOR PTF09AXC AND PTF09GE AND 900/4 FOR THE CIRCULAR BACKGROUND REGION FOR ASASSN–14AE).

Source	Background Power law index Γ	Background Flux erg cm^{-2} s^{-1}	Source model Power law index Γ	Source flux (absorbed; 0.3–7 keV) Flux erg cm^{-2} s^{-1}	Luminosity (0.3–7 keV) erg s^{-1}
PTF09axc	0.7±0.1	3.2×10^{-16}	2.5±0.1	$(8.5\pm0.5)\times10^{-13}$	$(3.2\pm0.2)\times10^{42}$
PTF09ge	0.3±0.2	3.7×10^{-16}	3.9±0.4	$(3.5\pm0.9)\times10^{-14}$	$3.9^{+1.1}_{-1.0}\times10^{41}$
ASASSN–14ae	–	–	3.2±1.0	$(1.8\pm0.8)\times10^{-14}$	$(9^{+9}_{-5})\times10^{40}$
PTF09djl	–	–	2.5*	$<3\times10^{-15}$	$<3\times10^{41}$

* Parameter fixed to this value. When using a 0.18 keV black body to convert the derived upper limit on the number of source photons to flux as same flux limit as reported for the power law spectral shape is obtained.

cally selected TDEs have stringent early–time X–ray upper limits around or below the luminosities seen in the three sources we detected at late times. For instance, Gezari et al. (2012) provide a non–detection for the optical/UV selected TDE PS1–10jh, with an upper limit to the 0.2–10 keV X–ray luminosity of $<5.8\times10^{41}$erg s^{-1}. Blagorodnova et al. (2017) report a marginal detection of the TDE iPTF16fnl in stacked observations with a 0.3–10 keV luminosity of $2.4^{+1.9}_{-1.1}\times10^{39}$erg s^{-1}, and Hung et al. (2017) did not detect the TDE iPTF16axa down to a 0.3–10 keV luminosity limit of $<3\times10^{41}$erg s^{-1}. As a caveat, we note that these reported upper limits were provided for the 0.2/0.3–10 keV band, whereas in Table 3, we report 0.3–7 keV luminosities. For spectral shapes with power-law index of 2 (typically assumed for the above cases), these upper limits would be 10–20% lower when converted to the 0.3–7 keV band.

The late–time detection of X–ray emission in PTF09axc, PTF09ge, and ASASSN–14ae provides further evidence against the alternative hypothesis that most claimed TDE candidates are, in reality, exotic nuclear supernovae (Saxton et al. 2018). Supernova (SNe) explosions are not generally bright in X–ray wavelengths, and even among those that are X–ray bright, none are observed to emit above $\sim10^{39}$ erg s^{-1} at times $\gtrsim10^{4}$ days post–peak (Dwarkadas & Gruszko 2012). This upper limit is far below even the late–time luminosity detected for ASASSN–14ae. Our observations complement late–time FUV detections of six TDE candidates (including PTF09ge) by van Velzen et al. (2018), which also argue against a "peculiar SNe" interpretation.

Our results also constrain the hypothesis that PTF09axc may represent extreme optical variability in a low-luminosity AGN. This interpretation was first raised in Arcavi et al. (2014), who observed a weak [O III] emission feature with luminosity $L_{\rm [O\ III]}=(2.4\pm0.3)\times10^{39}$ erg s^{-1}. This feature is not conclusive evidence of an AGN, and could also be produced by star formation, but in conjunction with the 2014 X–ray detection of the host galaxy, has cast doubt on the TDE status of PTF09axc (see e.g. Auchettl et al. 2017). Our X–ray luminosity measurement strengthens the case that PTF09axc is indeed a bonafide TDE. Using an empirical relationship between the [O III] and 3–20 keV luminosities in AGN (Heckman et al. 2005), we can estimate the range of [O III] line luminosities expected if our X–ray detection were of AGN origin (the scatter in this relationship is $\sigma=0.51$ dex, i.e. a factor ≈3.24). Converting our 0.3–7 keV luminosity to the 3–20 keV band using W3PIMMS, PTF09axc has an L_X (3-20 keV) of 8×10^{42}erg s^{-1}, and therefore the predicted AGN luminosity for the [O III] line would be $L_{\rm [O\ III]}\approx5.7\times10^{40}$erg s^{-1}, which is a factor ≈ 24 higher than the actual $L_{[\rm O\ III]}$ measured by Arcavi et al. (2014). The predicted value of $L_{[\rm O\ III]}$ is inconsistent with the observed value at the 2.7σ level, making a conventional AGN origin for the X-ray and [O III] luminosity unlikely.

The detected *Chandra* luminosities of PTF09ge and ASASSN–14ae can be compared with the late–time FUV luminosities reported for those sources by van Velzen et al. (2018). FUV detections of these sources were used to produce disk models and estimates for a range of quasi–thermal soft X–ray luminosities; the range of modeled X–ray predictions is particularly sensitive to the dimensionless SMBH spin parameter, $\chi_\bullet$. While our detection of ASASSN–14ae is compatible with the lower end (i.e. retrograde disk and large $|\chi_\bullet|$) of the predicted range $\log_{10}[L_{\rm X}/({\rm erg\ s^{-1}})] = 41.7^{+1.3}_{-0.9}$, our detection of PTF09ge is considerably brighter than the predicted range $\log_{10}[L_{\rm X}/({\rm erg\ s^{-1}})] = 37.0^{+3.6}_{-2.6}$ (van Velzen et al. 2018, where the fiducial predictions correspond to assuming $\chi_\bullet = 0$, and the lower and upper error bars correspond to assuming $\chi_\bullet = -0.9$ and $\chi_\bullet = 0.9$, respectively). This discrepancy could be reconciled by invoking even larger values of prograde SMBH spin and/or a SMBH mass somewhat smaller than the fiducial prediction of the $M_\bullet - \sigma$ relationship (Wevers et al. 2019a). Unfortunately, PTF09axc was not observed at late times in the FUV.

Interestingly, PTF09djl, which went undetected in the X–rays (with a 0.3–7 keV upper limit of $3 \times 10^{41}{\rm erg\ s^{-1}}$), was detected in the FUV at $3{\times}10^{42}$ erg s^{-1}, leading to a predicted X–ray luminosity range $\log_{10}[L_{\rm X}/({\rm erg\ s^{-1}})] = 41.5^{+1.6}_{-1.1}$. Our non–detection is compatible with this prediction for any range of retrograde SMBH spin values. While there are a number of important caveats associated with the late–time X–ray luminosity predictions from van Velzen et al. (2018), the strong sensitivity of quasi–thermal X–ray emission to $\chi_\bullet$ in late–time TDE disks underlines the value of multiwavelength, late–time observations for constraining SMBH spin. We will return to this subject in Section 3.4.

3.1. *Disk state changes*

Stellar–mass black holes that accrete from companion stars are visible as X–ray binaries. The X–ray emission from these disks exhibits a wide variety of spectral properties, or "states" (e.g. Hasinger & van der Klis 1989; Fender & Belloni 2004)[10]. Two of the most commonly observed states, the high–soft and low–hard state, are characterized by quasi–thermal and power–law spectra, respectively. Soft states often show sub–dominant power–law X–ray contributions from thermal seed photons up–scattered by an electron corona. One of the important variables controlling the accretion state of an XRB disk is the dimensionless mass accretion rate $\dot{m} \equiv \dot{M}/\dot{M}_{\rm Edd}$, where $\dot{M}$ is the physical accretion rate and $\dot{M}_{\rm Edd}$ is the Eddington–limited accretion rate. Because $\dot{M}$ in X–ray binary disks can vary greatly on humanly observable timescales, state changes are often observed, typically following a hysteresis pattern (Maccarone & Coppi 2003). When a source in a high–soft state experiences a persistent decline in $\dot{m}$, it will typically transition to a low-hard state once $\dot{m}$ falls below a threshold value ~ 0.03 (Maccarone & Coppi 2003). However, some variation in this transition luminosity (as a fractional Eddington luminosity) has been observed: Kalemci et al. (2013) find a soft–to–hard X–ray state change at an Eddington ratio of $\dot{m} = 0.0030 \pm 0.0041$, and on the extreme end, Chauhan et al. (2019) find a recent outburst of the candidate black hole XRB MAXI J1535-571 in which the soft–to–hard spectral state change seems to occur at a fraction 1.2–$3.3{\times}10^{-5}$ of the Eddington luminosity (see also Maccarone 2003 for a discussion of variation in Eddington fraction for state changes in XRBs).

There is some evidence that analogous state changes occur in AGN accretion disks around SMBHs (e.g. Maccarone et al. 2003, and references therein). However, as the viscous times in AGN disks are typically much longer than reasonable observational baselines, it is not easy to observe state changes in AGN. A further difficulty is that in the soft X–rays, AGN spectra are generally dominated by power–law or reflection contributions. This is because the peak of the thermal blackbody disk emission occurs in the extreme UV, where observations are hindered by gas and dust extinction (although a soft spectral component can sometimes be discerned, e.g. Done et al. 2012).

Compared to standard AGN, TDE disks are probably more favorable laboratories for observing "scaled up" state changes around SMBHs (Giannios & Metzger 2011; Tchekhovskoy et al. 2014). The main reason is that the accretion disks expected to form in TDEs are much smaller than AGN disks, implying shorter time scales. If we consider a steady–state Shakura–Sunyaev disk with dimensionless viscosity α, constant aspect ratio H/R, and an outer edge $R_{\rm d}$, the viscous time scales as $\propto R_{\rm d}^{3/2}$. Late–time TDE disks should be geometrically thin and mostly circularized, and have an outer radius $R_{\rm d} \sim 2R_{\rm p} = 2R_{\rm t}/\beta$, where $\beta \sim 1$ is the penetration parameter of the TDE, and the tidal radius is

$$\begin{aligned} R_{\rm t} =& R_\star \left(\frac{M_\bullet}{M_\star}\right)^{1/3} \\ \approx& 2\times10^{-6}\ {\rm pc} \left(\frac{M_\bullet}{10^6 M_\odot}\right)^{1/3} \left(\frac{M_\star}{M_\odot}\right)^{-1/3} \left(\frac{R_\star}{R_\odot}\right). \end{aligned} \quad (1)$$

Here $M_\star$ and $R_\star$ are the mass and radius of the victim star, and we see that both $R_{\rm t}$ and $R_{\rm d}$ are far smaller than the typical radius of an AGN accretion disk: for example, an AGN broad line region with 5100Å luminosity λL_λ has a typical scale $R_{\rm BLR} \approx 0.026\big(\frac{\lambda L_\lambda(5100\mathring{A})}{10^{44}}\big)^{0.7}$ pc (Kaspi et al. 2000), a factor of 10^4 times larger than the typical TDE disk.

Shortly after disruption, the peak mass fallback rate onto the SMBH will generally be super–Eddington, with a peak fallback rate $\dot{M}_{\rm peak} = \frac{1}{3}M_\star/t_{\rm fall}$, where

$$t_{\rm fall} \approx 3.5\times10^6\ {\rm s}\ \left(\frac{M_\bullet}{10^6 M_\odot}\right)^{1/2} \left(\frac{M_\star}{M_\odot}\right)^{-1} \left(\frac{R_\star}{R_\odot}\right)^{3/2} \quad (2)$$

[10] Formally, both timing and spectral properties are necessary for the identification of states (Hasinger & van der Klis 1989). Regrettably, the low number of detected X-ray photons in our late-time TDE observations precludes us from a meaningful X–ray timing study.

is the fallback time for the most tightly bound debris. In Eddington units, this is (Stone et al. 2013)

$$\frac{\dot{M}_{\rm peak}}{\dot{M}_{\rm Edd}} \approx 130 \left(\frac{M_\bullet}{10^6 M_\odot}\right)^{-3/2} \left(\frac{M_\star}{M_\odot}\right)^2 \left(\frac{R_\star}{R_\odot}\right)^{-3/2}. \quad (3)$$

If circularization is efficient, the disk accretion rate $\dot{M}$ will track the (super–Eddington) mass fallback rate, and therefore the most relevant stellar–mass point of comparison might seem to be ultra–luminous X–ray sources (ULXs), rather than high–soft XRBs (which are generally sub-Eddington). Contrary to this supposition, early–time soft X–ray detections of TDE candidates generally find quasi–thermal spectra that *are* analogous to a high–soft state (Komossa & Greiner 1999; Greiner et al. 2000), particularly in the best-characterized TDEs (Holoien et al. 2016a; Gezari et al. 2017; Wevers et al. 2019b), although we note that given the limited pass–band (typically 0.2–10 keV at best) it is difficult to rule out the soft ULX state (cf. Gladstone et al. 2009).

However, even in the limiting case of rapid circularization, the super–Eddington phase is expected to last only a fraction of the time TDEs are typically observed. Given the absence of observed state changes from a super–Eddington, ULX–like state to a sub–Eddington, high–soft state, we deem it likely that X–ray bright TDEs are seen mostly in the equivalent of the XRB soft state. As we will discuss in Section 3.2, the absence of super–Eddington emission may be related to a delay before the sources are detected in X–rays. A soft, quasi-thermal spectrum will no longer be a reasonable expectation (i) at late enough times, once $\dot{m}$ becomes very sub–Eddington, or (ii) if circularization is highly inefficient and $\dot{m} \ll 1$ always. Because $\dot{M}/\dot{M}_{\rm Edd}$ steadily decreases during late stages of a TDE flare, we may expect a late–time transition to the SMBH equivalent of the XRB low–hard state.

Observationally, TDE candidates with soft spectra containing an additional hard, power–law X–ray spectral components do exist (e.g. Holoien et al. 2016b; Saxton et al. 2017a,b), much like XRB soft states where a sub–dominant power-law component also exists. Another example is the X–ray selected TDE 2XMMi J184725.1−631724 (Lin et al. 2011). It showed an X–ray spectrum that was well–fit by a soft thermal component with a temperature of approximately 60 eV plus a (soft) power law with a photon index of around 3–4 contributing around 10–15% to the total 0.2–10 keV luminosity (at the first detection of the outburst, in Sept 2006). The temperature of the soft component had risen to around 90 eV nine months later as measured by *XMM–Newton*, with a power–law contribution of 5–10%. The X–ray spectrum in the TDE candidate RX J1242−1119 changed from a power–law with $\Gamma \approx 5$ (so a very soft spectrum that could also be fit with a blackbody with a temperature of 0.06 keV) to $\Gamma \approx 2.5$ at late–times (Komossa & Greiner 1999; Komossa et al. 2004), signifying a potential state change.

These exceptions aside, the best–studied TDE X–ray spectra are qualitatively closer to an XRB high–soft state than they are to AGN power laws. The reasons for this are unclear, but likely involve the higher blackbody temperature of TDE disks near the ISCO, due to (i) the smaller SMBH masses in TDEs relative to most AGN (compare the SMBH mass distributions in Woo & Urry 2002; Wevers et al. 2017, 2019a); (ii) the higher early–time Eddington fraction expected for TDEs in comparison to typical AGN (Kauffmann & Heckman 2009); (iii) a bias towards prograde spinning SMBHs for X–ray selected TDEs (see § 3.3) enabling a smaller value for the innermost stable circular orbit (ISCO). Early–time TDE X–ray spectra often appear even more thermally dominated than the typical XRB high–soft state, possibly indicating difficulty in forming a Compton scattering corona.

Our interpretation of the spectral properties of PTF09axc and PTF09ge follows straightforwardly from the XRB analogy: PTF09axc has undergone a state change to the SMBH analogue of the low–hard state, but this type of change has not yet occurred for PTF09ge, which likely remains in an analogue of the high–soft state. This hypothesis is complicated by the Eddington ratios we observe. Using literature estimates for the SMBH masses (Wevers et al. 2019a) and accounting for both the one–sigma scatter of the underlying $M_\bullet - \sigma$ relation and the uncertainty in our X-ray luminosity estimates, we find that PTF09axc was observed at an Eddington fraction of $\dot{m} = 5.4^{+12}_{-3.8} \times 10^{-2}$; PTF09ge was observed at an Eddington fraction of $\dot{m} = 1.6^{+3.3}_{-1.1} \times 10^{-3}$; and ASASSN–14ae at $\dot{m} = 2.8^{+13}_{-2.4} \times 10^{-3}$. The simplest theoretical expectation might be that the TDE disk with the lower Eddington ratio, PTF09ge, should have undergone a state change prior to one with a higher Eddington ratio (PTF09axc). However, we note that in XRBs, the emergence of a coronal power–law and the ensuing state change is regulated not only by the accretion rate $\dot{m}$ but also by an additional parameter (cf. Homan et al. 2001, where the second parameter is interpreted as the fractional size of the Comptonizing region). Furthermore, TDEs differ from standard accretion disks in several ways, and there are other plausible "hidden variables" that may be acting to prevent the emergence of a corona in PTF09ge. For example, the relatively weak magnetic fields of main sequence stars may mean that TDE disks are born with extremely low magnetizations[11]. Since coronal electron populations are thought to be accelerated to relativistic energies in magnetic reconnection events (Merloni & Fabian 2001), standard low–hard state coronae may only emerge in TDE disks born with unusually large magnetizations, or ones where external factors like large and retrograde SMBH spin (Parfrey et al. 2015) favor magnetic field generation *in situ* through dynamo processes.

Overall, the X–ray Eddington ratio of PTF09axc is broadly compatible with the common range of Eddington ratios where soft–to–hard state changes occur in XRBs. The persistently soft spectrum of PTF09ge is more unusual, but as mentioned before, XRB soft states have been observed to persist down to an Eddington ratio of $\sim 10^{-3}$ and in an extreme case even down to a few times 10^{-5}.

One testable prediction of our XRB analogy is the pre-

[11] Indeed, TDE disks may be so starved of magnetic flux that initial angular momentum transport may be dominated by exotic processes such as the Papaloizou-Pringle instability (Nealon et al. 2018) or fallback shocks (Chan et al. 2019) rather than the usual magnetorotational instability.

dicted radio luminosity using the Fundamental Plane of black hole activity (Merloni et al. 2003; Falcke et al. 2004). Using the calibration of Merloni et al. (2003), and given the SMBH mass estimate of $\log M_\bullet = 5.68$ in PTF09axc from Wevers et al. (2017), we derive an expected radio luminosity at 5 GHz of 2×10^{37}erg s^{-1}. Given the luminosity distance of PTF09axc, this translates to a flux density at 5 GHz of 20 μJy, a level which is detectable with current radio telescopes, although this flux estimate carries a substantial uncertainty.

If the soft X–ray spectra of X–ray bright TDEs imply that those systems accrete in the equivalent of the XRB soft state, the fact that many TDEs have very weak or nonexistent early-time radio emission is unsurprising (cf. Maccarone et al. 2003; van Velzen et al. 2013). We note that XMMSL1 J074008.2−853927, another TDE with an X–ray power–law component (index $\Gamma = 2$) was detected in radio (Saxton et al. 2017a; Alexander et al. 2017), although XMMSL2 J144605.0+685735, which shows a power–law with index $\Gamma = 2.5$, was not (Saxton et al. 2019 in prep.).

Finally, we note that our X–ray detections demonstrate that late–time TDE disks do not generally exhibit a different sort of state change: a collapse into a cold, gas pressure–dominated state due to the development of a thermal instability. This type of collapse is predicted by simple applications of the popular α–disk model, but would imply that late–time TDE disks have luminosities far below what we observe (Shen & Matzner 2014). Our observations further substantiate this point, which was recently made in the context of late–time detections of TDE disks in the FUV (van Velzen et al. 2018). The evidence against very cold disks in (most) TDEs seen at late times could indicate that the nonlinear development of the thermal instability is suppressed by an iron opacity bump (Jiang et al. 2016), or alternatively magnetic pressure support (Begelman & Pringle 2007; Sądowski 2016; Jiang et al. 2019).

3.2. *Optical vs. X–ray selected TDEs*

Many of the first TDE candidates were detected from their soft X–ray emission, but either lacked contemporaneous searches for optical variability (Komossa & Greiner 1999), or were observed *not* to show variable optical behavior (Greiner et al. 2000; Saxton et al. 2012; Saxton et al. 2019 in prep). Later, optical and UV surveys discovered a second class of TDE candidates, which often possessed upper limits on their X–ray emission (Gezari et al. 2012; see also PTF09ge, ASASSN–14ae, and PTF09djl). More recently, a number of TDEs have been observed to exhibit both optical/UV *and* X–ray variability (Holoien et al. 2016a,b; Wevers et al. 2019b). With such a diversity of X–ray ($L_{\rm X}$) and optical ($L_{\rm opt}$) luminosities, it is fair to ask: do these transients all really stem from the same underlying type of event?

In the context of the reprocessing paradigm, this question has sometimes been answered (theoretically) in the affirmative by introducing a viewing angle dependence, akin to the AGN unification model (Metzger & Stone 2016; Dai et al. 2018; Lu & Bonnerot 2019): edge–on TDEs obscure the X–rays from the inner accretion flow, but face–on TDEs are viewed through a low–density polar region, and thus will be X–ray bright. The complicated three–dimensional geometry of the circularization/shock paradigm (Piran et al. 2015; Shiokawa et al. 2015) likely suggests a viewing angle dependence as well.

A different – possibly complementary – way to unify TDE candidates across a broad range of $L_{\rm X}/L_{\rm opt}$ ratios is to postulate a strong temporal, rather than angular, dependence in $L_{\rm X}/L_{\rm opt}$. Our late–time detections of PTF09axc, PTF09ge, and ASASSN–14ae demonstrate that a substantial fraction of optically selected TDEs are X–ray bright at late times $\approx 5-10$ yr post–peak, signifying the presence of an exposed, compact accretion disk. If the optical emission is caused by circularization shocks, a delay between optical and X–ray would be related to delays in forming the (inner, X–ray emitting) accretion disk, as has been suggested by Shiokawa et al. (2015). If the optical is instead caused by reprocessing of the inner disk's X–rays and EUV, then an enshrouded inner disk will only become visible in X–rays after the reprocessing screen has diluted enough to permit an ionization breakout (Metzger & Stone 2016; Roth et al. 2016).

Because the low $L_{\rm X}$ values we observe are compatible with past X–ray non–detections (or, in the case of PTF09axc, its 2014 detection), we are unable to say whether this truly represents *brightening* of initially X–ray dim TDEs. However, deep limits on the X–ray luminosity in several other optically selected TDEs suggests that brightening is certainly plausible (for references and limits see the first paragraphs of the Discussion). The nature of the X–ray light curve in optically selected TDEs is a crucial observable to constrain with future observations. The offset between the peaks of optical and X–ray emission, Δt_{o-X}, is a key parameter for testing the idea of unification in *time*, rather than (or in addition to) angle. The distributions of Δt_{o-X} will depend on the emission mechanism for the optical and X–ray light, as well as on event parameters such as β, $M_\bullet$, and $\chi_\bullet$.

Depending on the delay between disruption and X–ray observation, an individual TDE could be in the equivalent of the soft X–ray spectral state, or as in the case of XMMSL2 J144605.0+685735, in a hard power–law like spectrum[12]. We hypothesize that the X–ray selected TDEs are, in this scenario, often discovered much longer after the disruption than are optically selected TDEs. This particular unification hypothesis would be falsified if observations months to years before the X–ray turn–on in a TDE candidate did not show signs of an optical enhancement[13].

This scenario also implies that all optically selected TDEs will at some point emit X–ray radiation, as is true for three of the four sources we observed in this work. Sources which are detected in both optical and X–ray observations at early times (e.g. ASASSN–14li, ASASSN–15oi and AT2018fyk; Holoien et al. 2016a, Holoien et al. 2016b, Wevers et al. 2019c, respectively) could be explained in this scenario as sources with efficient circularization due, for instance, to high β, large $M_\bullet$ (though this is disfavored by $M_\bullet - \sigma$ estimates), or large and ret-

[12] A potential selection effect might be at play, as massive brightening of an X-ray power law is more difficult to separate from AGN flares, and thus will often not be classified as a TDE, but as an AGN flare

[13] In individual host galaxies, there could be reasons why the optical emission should be strongly reduced in these TDEs (such as the presence of a large amount of nuclear dust, e.g. Mattila et al. 2018).

rograde SMBH spin.

The shape of the X–ray spectra as well as the lower luminosities that we observed in PTF09axc, PTF09ge and ASASSN–14ae differ from the (soft) X–ray discovered TDEs, which have soft thermal spectra and luminosities of order $L_X \approx 10^{43-44}$erg s^{-1} (Auchettl et al. 2017). This implies that our observed sources are, in this scenario, at an even later stage in the evolution of the mass fall–back and accretion rate.

3.3. *Rates of detection in future X–ray surveys*

Near–future wide–field X–ray surveys are predicted to expand our sample of X–ray TDEs by $1-2$ orders of magnitude. For example, the Einstein Probe is expected to find ~ 100 new TDEs per year (Yuan et al. 2015), while eROSITA is expected to find ~ 1000 (Khabibullin et al. 2014). In this section, we revisit the latter estimate, making the following modifications to the model of Khabibullin et al. (2014):

1. We allow (in one of our models) the temperature at the inner edge of the accretion disk to be a function of SMBH spin.
2. We assume the volumetric TDE rate is given by:

$$\dot{N}_{\rm tde} = 2.9\times10^{-5}\left(\frac{M_\bullet}{10^8 M_\odot}\right)^{-0.4} {\rm yr}^{-1}\phi(M_\bullet). \quad (4)$$

   This assumption takes a theoretical (per galaxy) TDE rate calibrated from observations of nearby galactic nuclei (Stone & Metzger 2016), and multiplies this by $\phi(M_\bullet)$, the $z = 0.02$ black hole mass function from Shankar et al. (2009) (their table 3).[14] We consider black hole masses between $10^5 M_\odot$ and $10^8 M_\odot$ in our estimate. The volumetric TDE rate is $\sim 10^{-5}$ Mpc^{-3} yr^{-1} for this range.

We consider two different models for the TDE light curve and spectrum: (I) an optimistic theoretical model based on simple accretion disk theory and (II) a more pessimistic quasi–empirical model that is calibrated to reproduce the late–time X–ray properties of PTF09ge. In both cases, we only consider disruption of Solar–type stars, for simplicity.

3.3.1. *Model I*

We assume circularization occurs efficiently, and that the mass accretion rate through the disk is

$$\dot{M}_{\rm acc}(M_\bullet, t) = \begin{cases} 0 & t < t_{\rm fall} \\ \dot{M}_{\rm max}(M_\bullet)\left[\frac{t}{t_{\rm fall}(M_\bullet)}\right]^{-1.2} & t \geq t_{\rm fall} \end{cases} \quad (5)$$

where $t_{\rm fall}$ is the fallback time (Eq. 2). This power law is shallower than the canonical $t^{-5/3}$ decline of the mass fall–back rate and is motivated by theoretical models for viscously spreading disks (Cannizzo et al. 1990), the late time FUV light curves of TDEs (van Velzen et al. 2018), and our own late–time X–ray detections. The maximum accretion rate $\dot{M}_{\rm max}$ is a factor of $\sim$3 smaller than the peak fall–back rate $\dot{M}_{\rm peak}$. With this normalization, a total of half a solar mass of material is accreted.

The bolometric disk luminosity after one fallback time is

$$L_{\rm bol}(t, M_\bullet, \chi_\bullet) = \min[L_{\rm Edd}(M_\bullet), \eta_\bullet(\chi_\bullet)\dot{M}_{\rm acc}(t)c^2]$$
$$= \min\Big[L_{\rm Edd}(M_\bullet),$$
$$3\times10^{45}\left(\frac{\eta_\bullet(\chi_\bullet)}{0.057}\right)\left(\frac{M_\bullet}{10^6 M_\odot}\right)^{-1/2}\left(\frac{t}{t_{\rm fall}}\right)^{-1.2} {\rm erg\ s}^{-1}\Big], \quad (6)$$

where $L_{\rm Edd}(M_\bullet)$ is the Eddington luminosity, and $\eta_\bullet$ is the standard radiative efficiency of a thin, equatorial accretion disk[15]. Here we have further assumed that the disk aligns itself into the SMBH equatorial plane after an initial period of misalignment. Typical alignment timescales are $\lesssim 100$ d for large ($\chi_\bullet > 0.5$) SMBH spins (Franchini et al. 2016), so alignment is a reasonable approximation for eROSITA observations, which have a typical cadence of 6 months[16]. Eq. (6) is close to the estimated bolometric luminosity of PTF09ge near peak ($\sim 8\times10^{44}$ erg s^{-1}, which is comparable to the Eddington limit for this source; see van Velzen et al. 2018).

Equations (5) and (6) specify the bolometric luminosity, but here we are interested in soft X–ray observations of TDEs, and many optically selected TDEs (including three sources of our sample) have not been detected in X–rays at early times. Theoretically, TDEs may become X–ray bright when the central engine ionizes through a surrounding reprocessing layer (Metzger & Stone 2016; Roth et al. 2016) or, if circularization is inefficient, after repeated shock interactions near stream apocenter (e.g. Dai et al. 2015; Shiokawa et al. 2015). The precise time when this occurs is uncertain. However, at least the early, super–Eddington phases of mass fallback are likely to be X–ray dim.[17] If disk formation is inefficient, there is little accretion to produce X–rays (Shiokawa et al. 2015); even if disk formation is efficient, the inner disk can be heavily obscured by bound debris (Loeb & Ulmer 1997; Coughlin & Begelman 2014) or by outflows (Miller 2015; Metzger & Stone 2016; Dai et al. 2018; Lu & Bonnerot 2019). However, as our present work shows, a large fraction of TDEs become X–ray bright at later times, when the luminosity becomes sub–Eddington. This occurs after

$$t_{\rm Edd}(M_\bullet, \chi_\bullet) \approx 1.5{\rm yr}\left(\frac{M_\bullet}{10^6 M_\odot}\right)^{-3/4}\left(\frac{\eta(\chi_\bullet)}{0.057}\right)^{5/6}. \quad (7)$$

Here, $t_{\rm Edd}$ is the time after which the accretion rate becomes sub–Eddington. In practice, we consider a TDE at redshift z to be detectable by eROSITA after

[14] eROSITA would be sensitive to TDEs with $z \lesssim 0.2$, and the Shankar et al. (2009) mass function varies little in this redshift range.

[15] The efficiency $\eta_\bullet$ ranges from 0.038 to 0.42 as $a_\bullet$ goes from -1 to 1, and is computed as in Bardeen et al. (1972).

[16] In principle, alignment can take longer than 6 months if $\chi_\bullet \lesssim 0.5$, but $\eta_\bullet$ is considerably less sensitive to SMBH spin in this regime.

[17] At least for most viewing angles: observers aligned with the poles may see X–ray emission from a jet according to the unification model of Dai et al. 2018.

$t_{\rm Edd}(M_\bullet, \chi_\bullet)$, as long as

$$\frac{L}{4\pi d_L^2(z)K(z)} \geq f_{\rm lim}, \tag{8}$$

where $d_L(z)$ is the luminosity distance and

$$f_{\rm lim} = \frac{C_{\rm crit}}{t_{\rm int}\int_{\nu_{\rm min}}^{\nu_{\rm max}} \frac{S_\nu(\nu)A(\nu)e^{-\xi(\nu)}}{h\nu}{\rm d}\nu}$$
$$K(z)^{-1} = \frac{(1+z)\int_{\nu_{\rm min}}^{\nu_{\rm max}} \frac{S_\nu(\nu(1+z))A(\nu)e^{-\xi(\nu)}}{h\nu}{\rm d}\nu}{\int_{\nu_{\rm min}}^{\nu_{\rm max}} \frac{S_\nu(\nu)A(\nu)e^{-\xi(\nu)}}{h\nu}{\rm d}\nu} \tag{9}$$

Here $C_{\rm crit}$ and $t_{\rm int}$ are the minimum number of counts resulting in a detection and the integration time respectively (which we take to be 40 and 240 seconds following Khabibullin et al. 2014), A_ν is the effective area as a function of energy[18], $e^{-\xi(\nu)}$ accounts for photoelectric absorption[19], and S_ν is the Spectral Energy Distribution (SED), which we take to be a black–body with an effective temperature corresponding to the temperature near the ISCO as given by Eq. 9 of Lodato & Rossi (2011).[20] We integrate SEDs between $h\nu_{\rm min} = 0.2$ keV and $h\nu_{\rm max} = 2$ keV (following Khabibullin et al. 2014).

The total number of new TDEs detected every year is

$$N_{\rm det} = \int_0^{1\ \rm year}\int_{M_{\rm min}}^{M_{\rm max}}\int_0^{z_{\rm lim}(M_\bullet)} \frac{{\rm d}N}{{\rm d}t{\rm d}M_\bullet{\rm d}z}{\rm d}z{\rm d}M_\bullet{\rm d}t$$
$$= \int_0^{1\ \rm year}\int_{M_{\rm min}}^{M_{\rm max}}\int_0^{V_{\rm c}[z_{\rm lim}(M_\bullet)]} \dot{N}_{\rm tde}{\rm d}V_{\rm c}(z){\rm d}M_\bullet{\rm d}t, \tag{10}$$

where ${\rm d}N/{\rm d}t{\rm d}M_\bullet{\rm d}z$ is the differential TDE rate per unit SMBH mass per unit redshift, and $z_{\rm lim}$ is the maximum redshift to which a TDE in a given mass bin could be detected. In the second line, $\dot{N}_{\rm tde}$ is the volumetric TDE rate (Eq. 4), while ${\rm d}V_c$ is the co–moving volume element. Conservatively, $z_{\rm lim}$ satisfies

$$\frac{L(t_o + 6\ \rm months)}{4\pi d_L(z_{\rm lim})^2 K(z_{\rm lim})} = f_{\rm lim}$$
$$t_o = \max[t_{\rm edd}(M_\bullet, \chi_\bullet), t_{\rm fall}], \tag{11}$$

where t_o is when the X–rays turn on and six months is the time it takes eROSITA to scan the entire sky.

The top panel of Fig. 2 shows the eROSITA detection rate as a function of SMBH mass and spin, assuming all TDE hosts have the same mass and spin combination, and that the total TDE rate is 10^{-5} Mpc^{-3} yr^{-1}. For a flux–limited sample of TDEs produced by rapidly spinning black holes, there are 1–2 orders of magnitude more detections when the black hole spin is universally prograde (with respect to the accretion disk's rotation) than universally retrograde, irrespective of the SMBH mass bin we consider. In stark contrast to optically selected TDE samples (§ 3.4), an X–ray selected sample would be strongly biased towards prograde black hole spins, though this bias abates if the SMBH spin distribution is very bottom–heavy (with typical $\chi_\bullet \ll 1$).

In the bottom panel of Fig. 2, we use the more realistic, non–uniform (in SMBH mass) TDE rate given by Eq. 4. Smaller SMBH masses are strongly favored in flux–limited X–ray TDE samples, because (i) their disks have higher effective temperatures, increasing the luminosity in the eROSITA band; (ii) they preferentially occur in denser and cuspier galactic nuclei, where two–body relaxation times are shorter and TDE rates are higher; (iii) such SMBHs are more common, given our assumed mass function. Our predictions are closest to those of Khabibullin et al. (2014) when we set $\chi_\bullet \approx 0.9 - 0.95$, where the effective temperature at the inner disk edge in our model matches theirs. The observed black hole mass distribution of soft X–ray selected TDEs (Wevers et al. 2019a) does not show evidence for a larger number of TDEs from smaller SMBH masses, although there is a hint for this in hard X–ray selected TDEs.

Table 4 shows the mass–integrated eROSITA detection for a few different SMBH spin parameters (assuming equal intrinsic numbers of prograde and retrograde disruptions). The detection rate is a strong function of the uncertain SMBH spin distribution: in our fiducial model (where the SMBH mass function extends down to $M_\bullet = 10^5 M_\odot$) we predict ≈1000 detections per year for $\chi_\bullet$=0.99, but only 170 per year for $\chi_\bullet = 0$. For large values of $\chi_\bullet$, a flux-limited sample is strongly dominated by the 50% of TDE disks we assume to align into prograde equatorial configurations; depending on the combination of $M_\bullet$ and $\chi_\bullet$, this "prograde bias" can range from $\sim 10\%$ to multiple orders of magnitude. Prograde disks and high values of $|\chi_\bullet|$ are favored because of their higher bolometric luminosities and effective temperatures.

The X–ray discovery rate is dominated by the smallest ($M_\bullet \sim 10^5 M_\odot$) SMBHs, a part of parameter space where the SMBH occupation fraction is poorly constrained. Interestingly, a flux–limited and X–ray selected TDE sample can be a more sensitive probe of the bottom end of the SMBH mass function than a volume–complete TDE sample would be[21]. In our models, this is true for $\chi_\bullet \lesssim 0.9$, and is due to the fact that (unless most SMBHs are nearly extremal) X–ray emission is typically on the Wien tail of TDE disks, and is thus highly sensitive to populations of smaller SMBHs. Furthermore, the eROSITA TDE detection rate may also be a strong indicator of the SMBH spin distribution, even if the spins of individual TDE–hosting SMBHs cannot be measured. This is analogous to the manner in which statistical samples of TDEs may probe the SMBH spin distribution near the Hills mass (Kesden 2012), although not limited to the largest TDE hosts.

Many TDE light curves would be reasonably well–sampled with eROSITA. For example, for a 10^5 (10^6) $M_\odot$ SMBH with a spin of 0.99, prograde disruptions would be visible on average for 27 (5.3) years. This would give an average of eight detections per TDE, considering the cadence and nominal duration of the eROSITA all–sky survey (six months and four years respectively).

3.3.2. *Model II*

[18] https://wiki.mpe.mpg.de/eRosita/erocalib_calibration

[19] This is derived from the XSPEC PHABS multiplicative model with $N_H = 5 \times 10^{20}$ cm^{-2} following Khabibullin et al. (2014).

[20] The effective temperature actually goes to zero at the ISCO in this model. In practice we evaluate $T_{\rm eff,in}$ at 1.36 times the ISCO, where the effective temperature is maximized.

[21] Using Eq. 4, we find that reducing $M_{\rm min}$ from $10^6 M_\odot$ to $10^5 M_\odot$ increases the volumetric TDE rate by a factor ≈ 8.5.

TABLE 4
ESTIMATED eROSITA TDE DETECTION RATES.

	$\dot{N}(M_\bullet \geq 10^5 M_\odot)$			$\dot{N}(M_\bullet \geq 10^6 M_\odot)$		
$\chi_\bullet$	Total [yr^{-1}]	Retrograde [yr^{-1}]	Prograde [yr^{-1}]	Total [yr^{-1}]	Retrograde [yr^{-1}]	Prograde [yr^{-1}]
0	172.3	–	–	4.8	–	–
0.1	174.3	76.0	98.3	5.0	3.1	1.9
0.5	232.3	48.3	184.0	10.8	0.8	10.0
0.9	551.3	32.6	518.7	65.8	0.4	65.4
0.99	992.9	29.9	963.0	192.6	0.3	192.3

NOTE. — Estimated eROSITA TDE detection rates using the formalism outlined in § 3.3.1. The first column is the SMBH spin. Columns 2–4 give the total, retrograde, and prograde detection rates including all SMBHs between $10^5\ M_\odot$ and the Hills mass. Columns 5–7 give the total, retrograde, and prograde detection rate including SMBHs with masses between 10^6 and the Hills mass. In all cases we assumed an equal intrinsic number of prograde and retrograde disruptions (see the discussion in § 3.4). For these estimates, we assume the TDE mass function from Eq. (4), but discard TDEs with Galactic latitudes $\leq 30^\circ$, as in Khabibullin et al. (2014).

TABLE 5
ESTIMATED TDE DETECTION RATES WITH eROSITA USING THE QUASI-EMPIRICAL MODEL OUTLINED IN § 3.3.2.

$t_{\rm br}$ yr	$\dot{N}(M_\bullet \geq 10^5 M_\odot)$ [yr^{-1}]	$\dot{N}(M_\bullet \geq 10^6 M_\odot)$ [yr^{-1}]
1	150	24
5	16	2.6

Next, we re–estimate eROSITA detection rates with a quasi–empirical model calibrated to reproduce the observed properties of PTF09ge. While the model from the prior section was arguably an optimistic one (in its assumption that all TDEs will become X–ray bright after the disk accretion rate becomes sub-Eddington), this empirically calibrated model can be viewed as a rather pessimistic scenario, where we impose a long, adjustable period of X–ray darkness on most TDEs. In this model, the bolometric luminosity is

$$L_{\rm bol} = \begin{cases} 0 & , t \leq t_{\rm o} \\ \min\Big[L_{\rm Edd}(M_\bullet), 2.5\times10^{43}{\rm erg\ s^{-1}} \\ \left(\frac{t}{t_{\rm fall}}\right)^{-1.2}\left(\frac{M_\bullet}{3\times10^6 M_\odot}\right)^{-1/2}\Big] & , t \geq t_o. \end{cases}$$

$$t_o = \max[t_{\rm br}, t_{\rm Edd}, t_{\rm fall}] \quad (12)$$

This reproduces the inferred late–time bolometric luminosity for PTF09ge[22] for its inferred SMBH mass of $\sim 3\times10^6 M_\odot$ (Wevers et al. 2019a). The scalings with SMBH mass and time are the same as in the theoretical model, but SMBH spin is not explicitly included. The X–rays turn on after the brightening time ($t_{\rm br}$), as long as this is greater than the fallback time and the luminosity is sub–Eddington.

We assume, based on our late–time observations of PTF09ge, that the spectrum is a blackbody with effective temperature $kT = 0.18$ keV. The bolometric luminosity is up to two orders of magnitude smaller than in Model I, which would reduce the detection rate. However, this is partially compensated for by the harder spectrum.

Table 5 shows the mass–integrated eROSITA detection rates for two different brightening times $t_{\rm br}$. For higher SMBH minimum masses ($M_{\rm min} = 10^6 M_\odot$) and small brightening times, the rates are comparable to the estimates from Model I for moderate spins (with $0.5 \lesssim \chi_\bullet \lesssim 0.9$–see Table 4). However, the predicted rates for lower SMBH mass limits ($M_{\rm min} = 10^5 M_\odot$) and/or larger brightening times are smaller than the zero spin case in Model I.

In Model II, TDEs are on average observable for 2 (6) years after detection for a brightening time of 1 (5 years). This implies significantly poorer temporal sampling in eROSITA light curves than in Model I.

3.4. *Retrograde and prograde TDE disks*

In the previous section, we saw that X–ray selected TDE samples are likely to possess a strong bias towards prograde configurations of SMBH spin $\vec{\chi}_\bullet$ and disk angular momentum $\vec{L}_{\rm d}$ (i.e. $\vec{\chi}_\bullet \cdot \vec{L}_{\rm d} > 0$), so long as typical SMBH spin magnitudes are reasonably large ($\chi_\bullet \gtrsim 0.5$). In this section, we discuss prospects for observing this prograde preference, and build simple toy models to show how it contrasts with the likely weaker orientation biases in optically selected TDE samples, which may even exhibit a preference for retrograde configurations ($\vec{\chi}_\bullet \cdot \vec{L}_{\rm d} < 0$)

Our observations of PTF09ge indicate that quasi–thermal soft X–ray emission may remain visible for roughly a decade after the peak of a tidal disruption flare. This raises the prospect of using late–time TDE observations to directly measure SMBH spin through continuum fitting techniques. While continuum fitting is a fruitful method of measuring the spins of stellar–mass black holes in XRBs (McClintock et al. 2014), it has only rarely been applied to SMBHs because *(i)* AGN typically produce dusty tori, and these complicate the X–ray spectral fitting, *(ii)* the spectral peak of a quasi–thermal AGN disk is usually in observationally inaccessible EUV bands.

The relatively cool temperatures of TDE disks (in contrast to those of XRBs) mean that quasi–thermal soft X–rays will generally be on the Wien tail of emission (Lodato & Rossi 2011), and their production will be dominated by the innermost gas annuli of the disk. As a result, quasi–thermal X–rays from TDEs will be exponentially sensitive to the size of the disk inner edge, and therefore will depend strongly on SMBH spin. At early times, the disk inner edge is nontrivial to estimate. Because two–body scattering feeds stars to SMBHs from a roughly isotropic distribution of angles, TDE disks are generically born with order unity tilts. A tilted thin disk will be truncated near the innermost stable spherical orbit (ISSO), but the high early–time accretion rates of TDEs may cause their innermost disk annuli to extend inside the ISSO[23]. A greater problem at early times,

[22] 2.7×10^{41} erg s^{-1} derived from the best fit black body spectrum for this event.

[23] For example, with accretion disks tilted with respect to the

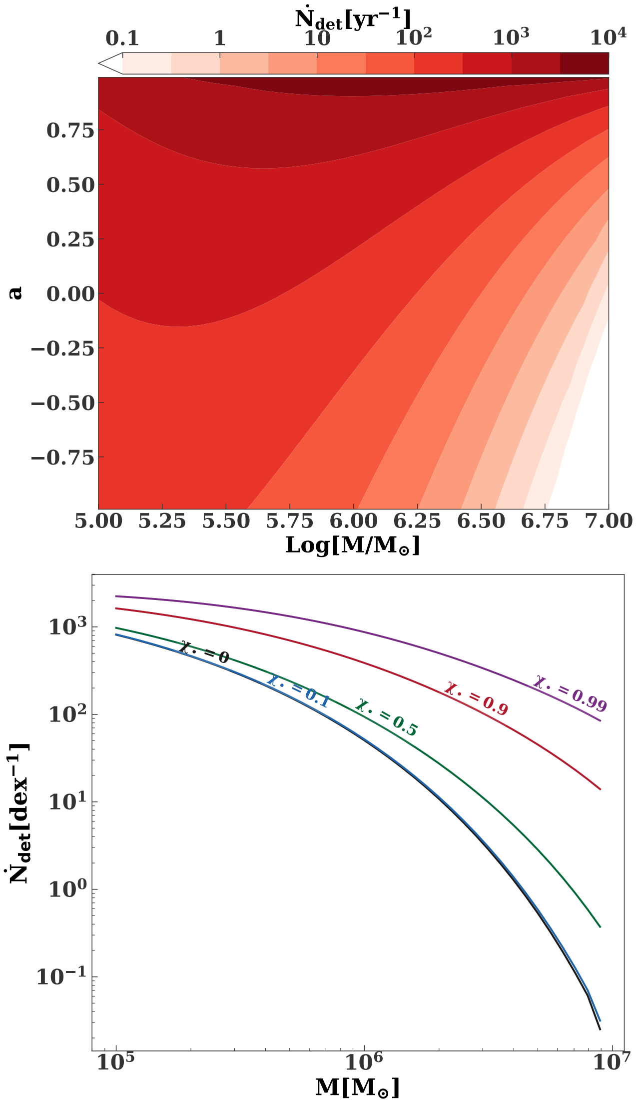

FIG. 2.— *Top panel:* The rate of eROSITA detections as a function of SMBH mass and spin, for a fixed TDE rate of 10^{-5} Mpc^{-3} yr^{-1}. These are the detection rates assuming TDEs are distributed as a delta function with a specific mass and spin (i.e. each SMBH mass and spin is assumed equally likely). *Bottom panel:* The rate of eROSITA detections as a function of SMBH mass, for a selection of spin parameters. These lines are a convolution of the rates from the top panel with the SMBH mass function and a theoretical estimate of TDE rates as a function of $M_\bullet$ (Eq. 4). We assume 50% of TDE disks align into prograde equatorial and 50% align into retrograde equatorial configurations by the time of observation–see the discussion in § 3.4).

however, is the messy hydrodynamical environment of the disk: if the stellar pericenter was sufficiently non–relativistic ($R_{\rm p} \gg R_{\rm g}$), the disk may retain substantial eccentricity (Shiokawa et al. 2015), and if optically thick stellar debris subtends a large solid angle on the sky, the majority of the X–ray flux may be absorbed in a reprocessing layer (Guillochon et al. 2014b; Metzger & Stone 2016).

At late times, however, accretion rates will have dropped to sub-Eddington levels, shifting the disk inner edge close to the test particle value; many fallback times will have passed, enabling more complete circularization (Hayasaki et al. 2016; Bonnerot et al. 2017); reprocessing layers will have dissipated, revealing the inner disk (Metzger & Stone 2016; van Velzen et al. 2018); and internal torques will have had time to align the TDE disk angular momentum vector with the black hole spin vector (Franchini et al. 2016). Thus, for the quasi-thermal sources we have observed (PTF09ge, and perhaps ASASSN–14ae), it is reasonable to expect thin disks in the SMBH equatorial plane, with inner edges at the test particle ISCO. We may now ask the question: do we expect an imbalance in the number of prograde and retrograde TDEs? For a volume–complete sample the answer is clearly no. However, for a more practical, flux–limited, sample of TDEs, there are strong reasons to suspect an imbalance. We have already predicted that flux-limited, X-ray selected TDE samples can exhibit an enormous prograde bias (e.g. Table 4). In this section, we investigate whether the same bias should be apparent for a flux-limited but optically selected TDE sample. While the origin of TDE optical emission remains contested between "shock-powered" and "reprocessing" models, both of these scenarios have peak luminosities that will depend strongly on the orbital precession of debris streams, and therefore on SMBH spin.

To leading post-Newtonian (PN) order, both apsidal precession (precession of the debris stream's Runge–Lenz vector within the orbital plane) and nodal precession (precession of the orbital plane's angular momentum vector about the SMBH spin vector) are larger for retrograde than for prograde orbits (Merritt et al. 2010). Neglecting for now the possibility that extreme nodal precession may prevent stream self-intersections[24], the greater apsidal shifts for debris from retrograde TDEs means that these debris streams will self-intersect and dissipate energy at smaller radii. Smaller stream self-intersection radii $R_{\rm SI}$ will probably yield higher peak optical luminosities, regardless of the dominant optical power source in observed TDEs. In the "reprocessing paradigm," smaller $R_{\rm SI}$ will mean faster disk formation and higher peak accretion rates $\dot{M}$ onto the SMBH, although this must be weighed against the potentially greater radiative efficiency of prograde disks. In the "circularization paradigm," smaller $R_{\rm SI}$ values will thermalize greater amounts of bulk kinetic energy.

The translation between self–intersection radius $R_{\rm SI}$ and optical luminosity is currently an unsolved problem. Under the assumption that most of the observed optical emission is shock-powered, we will use the following toy model for peak luminosity:

$$L_{\rm peak} = \eta_{\rm SI} \frac{GM_\bullet \dot{M}_{\rm peak}}{R_{\rm SI}}, \qquad (13)$$

where, as before, $\dot{M}_{\rm peak}$ is the peak mass fallback rate.

black hole spin by an angle 15° and a thickness of the order of 0.2, the simulations of Fragile (2009) found the inner edge to be nearly independent of spin.

[24] Tidal disruptions of stars in the relativistic regime (e.g. white dwarfs disrupted by intermediate–mass BHs, or solar mass main sequence stars disrupted by a BH with $M_\bullet = 10^{7-8}{\rm M}_\odot$) around spinning SMBHs, may lead to stellar debris streams that fail to promptly self–interact, unless the inclination of the stellar orbit is nearly perpendicular to the BH spin axis or if the thickness of the debris streams is large enough such that they always intersect (Dai et al. 2013; Guillochon & Ramirez-Ruiz 2015, Hayasaki et al. 2016).

The dimensionless number $\eta_{\rm SI} \leq 1$ is the fraction of stream kinetic energy thermalized *and* radiated at the self-intersection; for simplicity, we take it to be a constant[25]. A flux-limited survey will find a differential number of TDEs per bin of pericenter $R_{\rm p}$ and inclination i that scales as $\mathrm{d}N_{\rm det}/\mathrm{d}i\mathrm{d}R_{\rm p} \propto L_{\rm peak}^{3/2}(i,R_{\rm p})(\mathrm{d}\dot{n}/\mathrm{d}i\mathrm{d}R_{\rm p})$, where the differential rate $\mathrm{d}\dot{n}/\mathrm{d}i\mathrm{d}R_{\rm p} \propto \sin i$ if we are in the full loss cone (FLC) regime, and $\mathrm{d}\dot{n}/\mathrm{d}i\mathrm{d}R_{\rm p} \propto \sin i \times \delta(R_{\rm p}-R_{\rm t})$ if we are in the empty loss cone (ELC) regime (we have assumed isotropy in stellar arrival directions in both regimes).

The dependence of $L_{\rm peak}$ on i and $R_{\rm p}$ can be computed by defining the self-intersection radius (Dai et al. 2015)

$$R_{\rm SI} = \frac{R_{\rm p}(1+e)}{1+e\cos(\pi+\delta\omega/2)}, \tag{14}$$

where e is the eccentricity of the elliptical orbit of the stream of material formed by the disrupted star. For convenience, we take the eccentricity of the most tightly bound debris, $e_{\rm min} = 1 - 2(M_\star/M_\bullet)^{1/3}/\beta$. Here, we have made use of the per–orbit apsidal shift angle, $\delta\omega$, which, to lowest PN order in dimensionless SMBH spin, $\chi_\bullet$, is (Merritt et al. 2010)

$$\delta\omega = A_{\rm S} - 2A_{\rm J}\cos i, \tag{15}$$

where

$$A_{\rm S} = \frac{6\pi}{c^2}\left(\frac{GM_\bullet}{R_{\rm p}(1+e)}\right) \tag{16}$$

$$A_{\rm J} = \frac{4\pi\chi_\bullet}{c^3}\left(\frac{GM_\bullet}{R_{\rm p}(1+e)}\right)^{3/2}. \tag{17}$$

In the empty loss cone regime, for fixed SMBH mass and stellar properties, the retrograde fraction is simply

$$f_{\rm ret}^{\rm ELC} = \frac{\int_{\pi/2}^{\pi}\sin i[1+e\cos(\pi+\delta\omega/2)]^{3/2}\mathrm{d}i}{\int_0^{\pi}\sin i[1+e\cos(\pi+\delta\omega/2)]^{3/2}\mathrm{d}i}, \tag{18}$$

In the full loss cone (FLC) regime, a second integral is necessary:

$$f_{\rm ret}^{\rm FLC} = \frac{\int_{\pi/2}^{\pi}\sin i\int_{R_{\rm min}}^{R_{\rm t}} R_{\rm p}^{-3/2}[1+e\cos(\pi+\delta\omega/2)]^{3/2}\mathrm{d}R_{\rm p}\mathrm{d}i}{\int_0^{\pi}\sin i\int_{R_{\rm min}}^{R_{\rm t}} R_{\rm p}^{-3/2}[1+e\cos(\pi+\delta\omega/2)]^{3/2}\mathrm{d}R_{\rm p}\mathrm{d}i}. \tag{19}$$

Here $R_{\rm p}$ ranges from a maximum value of $R_{\rm t}$ down to a minimum value of $R_{\rm min}(\chi_\bullet, i)$. This minimum value, the innermost bound spherical orbit (IBSO), is computed from the Kerr geodesic equations (Bardeen et al. 1972). The IBSO is larger for retrograde spins, which (via Eq. 13) introduces a prograde bias.

We illustrate the overall orientation bias in flux–limited samples of shock–powered TDEs in Fig. 3. There is no bias when $\chi_\bullet = 0$ (as symmetry demands), but the bias becomes notable when $\chi_\bullet \gtrsim 0.5$. Interestingly, the bias is qualitatively different in the two regimes of loss cone repopulation. In the empty loss cone regime, there is almost no bias for $M_\bullet \lesssim 10^6 M_\odot$, but a moderate retrograde bias for larger SMBHs. In the full loss cone regime, there is a moderate prograde bias across all bins of $M_\bullet$. Since the empty loss cone regime predominates for high–mass SMBHs, and the full loss cone regime predominates for low–mass SMBHs (Stone & Metzger 2016), we expect that flux–limited, shock–powered TDE samples will exhibit a prograde bias for $M_\bullet \lesssim 10^{6.5} M_\odot$, and a retrograde bias at higher masses.

We may also consider a similar sort of toy model for the reprocessing picture of TDE optical luminosity, designed to illustrate the competition between disk formation (which is faster for retrograde orbits) and the radiative efficiency of a circularized accretion disk (which is higher for prograde orbits). Let us say that the peak optical luminosity in a reprocessing model is

$$L_{\rm peak} = \eta_\bullet \eta_{\rm r} \dot{M}_{\rm max} c^2, \tag{20}$$

where $\eta_\bullet$ is the standard radiative efficiency of a thin, equatorial accretion disk (see § 3.3), and the efficiency with which an optically thick reprocessing layer converts X–ray and extreme UV photons to optical emission is assumed (again, for simplicity) to be a constant, $\eta_{\rm r}$. Here $\dot{M}_{\rm max}$ does not represent the peak mass fallback rate to pericenter, $\dot{M}_{\rm max} = \frac{M_\star}{3}(t/t_{\rm fall})^{-5/3}$, but rather the peak accretion rate through the disk, which we parametrize as

$$\dot{M}_{\rm max} = \frac{M_\star}{2t_{\rm circ}}, \tag{21}$$

where we assume that the "circularization timescale", $t_{\rm circ}$, is a function only of the self–intersection radius, and is related to the fallback time for the most tightly bound debris as $t_{\rm circ} = t_{\rm fall}(R_{\rm SI}/R_{\rm g})^{\xi}$. This power–law parametrization of the disk formation timescale is crude, but will suffice to explore what types of disk orientation biases we expect if reprocessing is responsible for the observed optical emission. We find modified versions of the empty and full loss cone regime retrograde fractions:

$$\tilde{f}_{\rm ret}^{\rm ELC} = \frac{\int_{\pi/2}^{\pi}\sin i[1+e\cos(\pi+\frac{\delta\omega}{2})]^{3\xi/2}\eta_\bullet^{3/2}\mathrm{d}i}{\int_0^{\pi}\sin i[1+e\cos(\pi+\delta\omega/2)]^{3\xi/2}\eta_\bullet^{3/2}\mathrm{d}i}, \tag{22}$$

and

$$\tilde{f}_{\rm ret}^{\rm FLC} = \frac{\int_{\pi/2}^{\pi}\sin i\int_{R_{\rm min}}^{R_{\rm t}}\left(\frac{\eta_\bullet}{R_{\rm p}^{\xi}}\right)^{3/2}[1+e\cos(\pi+\frac{\delta\omega}{2})]^{3\xi/2}\mathrm{d}R_{\rm p}\mathrm{d}i}{\int_0^{\pi}\sin i\int_{R_{\rm min}}^{R_{\rm t}}\left(\frac{\eta_\bullet}{R_{\rm p}^{\xi}}\right)^{3/2}[1+e\cos(\pi+\frac{\delta\omega}{2})]^{3\xi/2}\mathrm{d}R_{\rm p}\mathrm{d}i}. \tag{23}$$

We illustrate the retrograde fractions in a flux–limited, reprocessing-powered TDE sample in Fig. 4. In contrast to our earlier shock–powered calculations, our toy model for reprocessing power almost always exhibits a *prograde* disk bias, as this configuration yields much higher radiative efficiencies. The detailed nature of the orientation bias depends on the power law index ξ encoding the dependence of circularization efficiency on $R_{\rm SI}$ (in this figure, we use $\chi = 0.5$). Very high values of ξ ($\gtrsim 2$) can create a retrograde bias in a sample of TDEs in the empty loss cone regime, but this level of sensitivity to $R_{\rm SI}$ is not suggested by existing hydrodynamical simulations of circularization (Hayasaki et al. 2016; Bonnerot

[25] As Lu & Bonnerot (2019) have noted, a large fraction of the thermalized stream kinetic energy may be lost to adiabatic degradation prior to the time it can be emitted. Because the fractional energy loss to PdV work depends on gas optical depth at $R_{\rm SI}$ and therefore on $M_\bullet$ and other parameters, the assumption of constant $\eta_{\rm SI}$ is crude. Deriving a more complete theoretical model is, however, beyond the scope of this work.

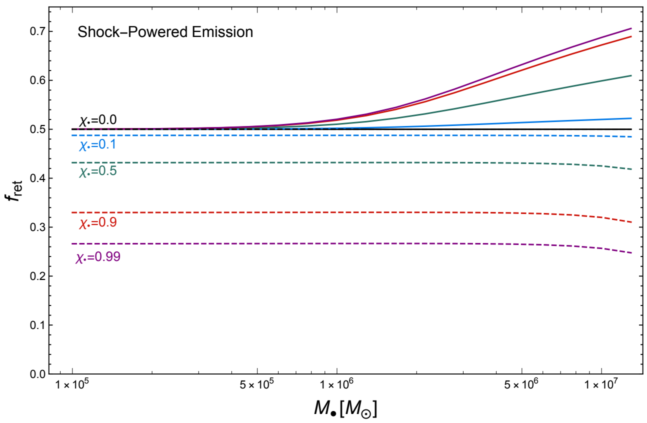

FIG. 3.— The fraction of TDEs with retrograde disks, $f_{\rm ret}$, in a flux-limited sample of (i) optically–selected and (ii) shock-powered tidal disruption flares. In the empty loss cone regime (solid lines), there is no preference for retrograde orbits when SMBH spin $\chi_\bullet$ is zero (the Schwarzschild limit), but the preference becomes more notable for higher values of $\chi_\bullet$ (shown and labeled as color-coded curves). Conversely, in the full loss cone regime (dashed lines), the preference is for prograde disks.

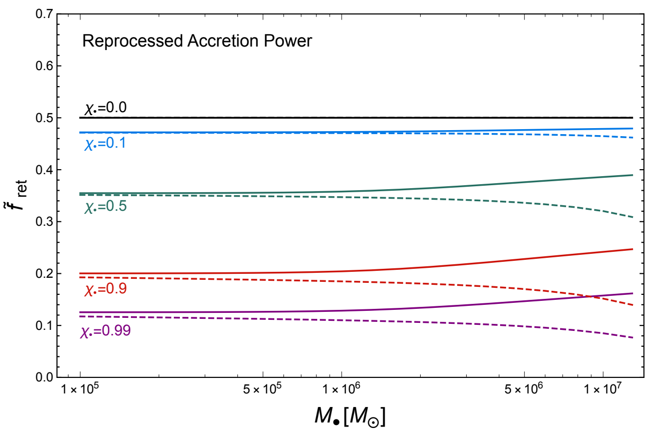

FIG. 4.— Same as Fig. 3, but we now compute the retrograde fraction ($\tilde{f}_{\rm ret}$) considering a model for optical emission based on reprocessed X-ray/EUV emission from an inner accretion disk. In contrast to the shock–powered model of Fig. 3, reprocessing-powered TDEs almost always show a bias for *prograde* disks due to radiative efficiency considerations. This bias is generally strongest for the empty loss cone regime and smaller SMBHs, but depends somewhat on the power law index ξ (assumed to be 0.5 in this plot). If $\xi \gtrsim 2$, a weak retrograde bias may be recovered in the empty loss cone regime.

et al. 2016). The overall level of bias depends on $\chi_\bullet$, but shows little variation with $M_\bullet$.

Of the TDEs we have observed, both PTF09ge and ASASSN–14ae have late–time accretion disks whose FUV properties were modeled in van Velzen et al. (2018). Our X–ray detections are compatible with these disk models provided the disk in PTF09ge is prograde with respect to a very rapidly spinning SMBH, and the disk in ASASSN–14ae is retrograde with respect to a spinning SMBH. While this sample is too small (and our disk models so far too crude) to meaningfully constrain $f_{\rm ret}$, these observations, and the arguments in this section, highlight the potential of future late–time observations and modeling to determine the dependence of peak flare luminosity on the inclination of the disrupted star's orbit. This may also serve as a useful test between different models of optical power sources in TDEs, as it would be hard to explain a pronounced retrograde bias in the reprocessing paradigm.

In this section, we have used simple but illustrative optical emission models to demonstrate that the selection effects operating in flux-limited, *optically selected* TDE samples favor a very different $\chi_\bullet$ distribution than do the selection effects in flux-limited, X–ray selected samples (§3.3). Specifically, an X–ray selected sample will be biased strongly towards prograde orbits around rapidly spinning SMBHs, while an optically selected sample will still be biased towards high $|\chi_\bullet|$, but much more weakly so, and may possess either a prograde or retrograde bias depending on the specific optical emission mechanism. A consequence of this is that the quasi-thermal X–ray luminosities in optically selected TDE distributions should be systematically lower than the corresponding X–ray luminosities in an X–ray selected sample, since the former will have cooler disk temperatures, on average.

4. CONCLUSIONS

We have conducted *Chandra* X–ray observations of four optically–selected TDEs long after the peak of their optical flares. In three cases we detected late–time soft X–ray emission: PTF09axc, PTF09ge, and ASASSN–14ae are best–fit with unabsorbed ($0.3-7$ keV) luminosities of $(3.2 \pm 0.2) \times 10^{42}$ erg s^{-1}, $3.9^{+1.1}_{-1.0} \times 10^{41}$ erg s^{-1}, and $9^{+9}_{-5} \times 10^{40}$ erg s^{-1}, respectively. Our fourth target, PTF09djl, was undetected by *Chandra*, yielding an upper limit on its soft X–ray luminosity of $L_{\rm X} < 3 \times 10^{41}$ erg s^{-1}. Three of these observations represent the longest temporal baseline for X–ray observations of optically–selected TDEs to date: PTF09axc and PTF09ge were observed roughly eight years after peak, while PTF09djl was observed roughly ten years post–peak.

These TDEs exhibit a diversity of X–ray behavior at late times. The X–ray spectrum of PTF09ge is best fit as the Wien tail of a thermal blackbody spectrum, similar to soft X–ray spectra observed at early times in optically–selected TDEs (and analogous to the high–soft state of XRBs). In contrast, the X–ray spectrum of PTF09axc is best fit as a comparatively hard, non–thermal power law, quite unlike most TDEs seen at early times, and more similar to the spectrum of an AGN or the low–hard state of an XRB. ASASSN–14ae does not have sufficient X–ray counts to determine the shape of its spectrum.

Our primary conclusions are as follows:

1. Late–time X–ray detections are further evidence that PTF09axc, PTF09ge, and ASASSN–14ae represent bonafide TDEs and not a peculiar type of nuclear supernova explosion. The persistence of high X–ray luminosities $\approx 5-10$ yr post-peak also argues strongly against the presence of a thermal instability in TDE disks, as would be predicted by simple α-disk theory.

2. We hypothesize that the marked spectral differences between PTF09axc and PTF09ge may have been caused by a late–time state change in PTF09axc to a low–hard state (in analogy to the state changes regularly observed in black hole X–ray binaries). Radio follow–up observations of PTF09axc could test this hypothesis, as could con-

tinued X–ray monitoring of PTF09ge to investigate if it also exhibits a state change to a power-law spectrum.

3. Assuming that our observations 4–9 years after optical detection are not caused by short–lived flares, we conclude that most TDEs are persistently bright X–ray sources visible for at least a decade, which has implications for detection rates in near future, wide field X–ray surveys. For example, we find the eROSITA instrument planned for imminent launch on the *Spectrum Röntgen Gamma* satellite could detect up to 1000 TDE flares per year if most low mass SMBHs have near maximal spins. However, the detection rate would be 170 per year if most SMBHs have zero spin, and (in the Schwarzschild limit) would be further reduced to only 5 per year if SMBHs with masses below $10^6 M_\odot$ are excluded.

4. We propose that there is often a delay between the peak optical and the X–ray emission in TDEs, such that optical and X–ray selected TDEs are, in many cases, the same type of flare observed at different stages. For example, in X–ray selected TDEs the optical emission (e.g. from the circularisation shock), may have already subsided below the level that can be detected above the nuclear region of the host galaxy.

5. The persistence of a soft X–ray spectrum at late times (such as in PTF09ge) opens up the possibility of black hole spin determinations using continuum fitting techniques (Wen et al. in prep.). These were, in the past, primarily applied to black holes in soft–state X–ray binaries (McClintock et al. 2014). Late–time X–ray observations will avoid, or at least minimize, theoretical uncertainties associated with early–time TDE disk modeling, such as generic disk tilts, significantly non–circular gas flows, and the presence of optically thick stellar debris on larger scales. The number of X–ray photons detected in the current observations of PTF09ge are, however, insufficient to attempt this exercise.

6. If the SMBHs responsible for TDEs possess appreciable spins, a flux–limited sample of TDEs will generally be biased towards an excess of prograde or retrograd disks. In an optically selected sample, the sign of this bias depends on the exact emission mechanism. Shock-powered optical emission (Piran et al. 2015) will exhibit a mild retrograde bias in the empty loss cone regime, and a mild prograde bias in the full loss cone regime. If instead, the optical emission is powered by reprocessed X–rays generated from a veiled inner accretion flow (Guillochon et al. 2014b; Metzger & Stone 2016), then prograde black hole spins are almost always favored, usually by a factor of a few. X–ray selected TDE samples have a very strong (one–to–two orders of magnitude) bias for prograde orbits if most SMBHs are spinning rapidly.

ACKNOWLEDGMENTS

We would like to thank the *Chandra X-ray Observatory* for approving and carrying out the observations presented in this paper. PGJ acknowledges funding from the European Research Council under ERC Consolidator Grant agreement no 647208 and discussions with Giacomo Cannizzaro. NCS and AG acknowledge funding from *Chandra* GO 18700591. NCS acknowledges additional funding from *Chandra* GO 20700515. BDM acknowledges support from NASA through the Astrophysics Theory Program (grant number NNX17AK43G). This research has made use of the NASA/IPAC Extragalactic Database (NED), which is operated by the Jet Propulsion Laboratory, California Institute of Technology, under contract with the National Aeronautics and Space Administration.

REFERENCES

Alexander, K. D., Wieringa, M. H., Berger, E., Saxton, R. D., & Komossa, S. 2017, ApJ, 837, 153
Arcavi, I., Gal-Yam, A., Sullivan, M., et al. 2014, ApJ, 793, 38
Auchettl, K., Guillochon, J., & Ramirez-Ruiz, E. 2017, ApJ, 838, 149
Bade, N., Komossa, S., & Dahlem, M. 1996, A&A, 309, L35
Bardeen, J. M., Press, W. H., & Teukolsky, S. A. 1972, ApJ, 178, 347
Begelman, M. C., & Pringle, J. E. 2007, MNRAS, 375, 1070
Berger, E., Zauderer, A., Pooley, G. G., et al. 2012, ApJ, 748, 36
Blagorodnova, N., Gezari, S., Hung, T., et al. 2017, ApJ, 844, 46
Bloom, J. S., Giannios, D., Metzger, B. D., et al. 2011, Science, 333, 203
Bonnerot, C., Rossi, E. M., & Lodato, G. 2017, MNRAS, 464, 2816
Bonnerot, C., Rossi, E. M., Lodato, G., & Price, D. J. 2016, MNRAS, 455, 2253
Bower, G. C., Metzger, B. D., Cenko, S. B., Silverman, J. M., & Bloom, J. S. 2013, ApJ, 763, 84
Cannizzo, J. K., Lee, H. M., & Goodman, J. 1990, ApJ, 351, 38
Cash, W. 1979, ApJ, 228, 939
Chan, C.-H., Piran, T., Krolik, J. H., & Saban, D. 2019, arXiv e-prints, arXiv:1904.12261. https://arxiv.org/abs/1904.12261
Chauhan, J., Miller-Jones, J. C. A., Anderson, G. E., et al. 2019, arXiv e-prints. https://arxiv.org/abs/1905.08497
Chornock, R., Berger, E., Gezari, S., et al. 2014, ApJ, 780, 44
Coughlin, E. R., & Begelman, M. C. 2014, ApJ, 781, 82
Dai, L., Escala, A., & Coppi, P. 2013, ApJ, 775, L9
Dai, L., McKinney, J. C., & Miller, M. C. 2015, ApJ, 812, L39
Dai, L., McKinney, J. C., Roth, N., Ramirez-Ruiz, E., & Miller, M. C. 2018, ApJ, 859, L20
Donato, D., Cenko, S. B., Covino, S., et al. 2014, ApJ, 781, 59
Done, C., Davis, S. W., Jin, C., Blaes, O., & Ward, M. 2012, MNRAS, 420, 1848
Dwarkadas, V. V., & Gruszko, J. 2012, MNRAS, 419, 1515
Evans, I. N., Primini, F. A., Glotfelty, K. J., et al. 2010, ApJS, 189, 37
Falcke, H., Körding, E., & Markoff, S. 2004, A&A, 414, 895
Farrar, G. R., & Gruzinov, A. 2009, ApJ, 693, 329
Farrar, G. R., & Piran, T. 2014, arXiv e-prints, arXiv:1411.0704. https://arxiv.org/abs/1411.0704
Fender, R., & Belloni, T. 2004, ARA&A, 42, 317
Fender, R. P., Belloni, T. M., & Gallo, E. 2004, MNRAS, 355, 1105
Fragile, P. C. 2009, ApJ, 706, L246
Franchini, A., Lodato, G., & Facchini, S. 2016, MNRAS, 455, 1946
Frank, J., & Rees, M. J. 1976, MNRAS, 176, 633
Garmire, G. P. 1997, in Bulletin of the American Astronomical Society, Vol. 29, Bulletin of the American Astronomical Society, 823–+
Generozov, A., Mimica, P., Metzger, B. D., et al. 2017, MNRAS, 464, 2481

Gezari, S., Cenko, S. B., & Arcavi, I. 2017, ApJ, 851, L47
Gezari, S., Martin, D. C., Milliard, B., et al. 2006, ApJ, 653, L25
Gezari, S., Heckman, T., Cenko, S. B., et al. 2009, ApJ, 698, 1367
Gezari, S., Chornock, R., Rest, A., et al. 2012, Nature, 485, 217
Giannios, D., & Metzger, B. D. 2011, MNRAS, 416, 2102
Gladstone, J. C., Roberts, T. P., & Done, C. 2009, MNRAS, 397, 1836
Greiner, J., Schwarz, R., Zharikov, S., & Orio, M. 2000, A&A, 362, L25. https://arxiv.org/abs/astro-ph/0009430
Guillochon, J., Manukian, H., & Ramirez-Ruiz, E. 2014a, ApJ, 783, 23
—. 2014b, ApJ, 783, 23
Guillochon, J., & Ramirez-Ruiz, E. 2013, ApJ, 767, 25
—. 2015, ApJ, 809, 166
Hasinger, G., & van der Klis, M. 1989, A&A, 225, 79
Hayasaki, K., Stone, N., & Loeb, A. 2016, MNRAS, 461, 3760
Heckman, T. M., Ptak, A., Hornschemeier, A., & Kauffmann, G. 2005, ApJ, 634, 161
Helene, O. 1984, Nuclear Instruments and Methods in Physics Research A, 228, 120
Hills, J. G. 1975, Nature, 254, 295
Holoien, T. W.-S., Prieto, J. L., Bersier, D., et al. 2014, MNRAS, 445, 3263
Holoien, T. W.-S., Kochanek, C. S., Prieto, J. L., et al. 2016a, MNRAS, 455, 2918
—. 2016b, MNRAS, 463, 3813
Homan, J., Wijnands, R., van der Klis, M., et al. 2001, ApJS, 132, 377
Hung, T., Gezari, S., Blagorodnova, N., et al. 2017, ApJ, 842, 29
Hung, T., Gezari, S., Cenko, S. B., et al. 2018, ApJS, 238, 15
Jiang, Y.-F., Blaes, O., Stone, J., & Davis, S. W. 2019, arXiv e-prints. https://arxiv.org/abs/1904.01674
Jiang, Y.-F., Davis, S. W., & Stone, J. M. 2016, ApJ, 827, 10
Jonker, P. G., Heida, M., Torres, M. A. P., et al. 2012, ApJ, 758, 28
Kalemci, E., Dinçer, T., Tomsick, J. A., et al. 2013, ApJ, 779, 95
Kaspi, S., Smith, P. S., Netzer, H., et al. 2000, ApJ, 533, 631
Kauffmann, G., & Heckman, T. M. 2009, MNRAS, 397, 135
Kesden, M. 2012, Phys. Rev. D, 85, 024037
Khabibullin, I., Sazonov, S., & Sunyaev, R. 2014, MNRAS, 437, 327
Kim, M., Kim, D.-W., Wilkes, B. J., et al. 2007, ApJS, 169, 401
Komossa, S., & Bade, N. 1999, A&A, 343, 775. https://arxiv.org/abs/astro-ph/9901141
Komossa, S., & Greiner, J. 1999, A&A, 349, L45. https://arxiv.org/abs/astro-ph/9908216
Komossa, S., Halpern, J., Schartel, N., et al. 2004, ApJ, 603, L17
Kraft, R. P., Burrows, D. N., & Nousek, J. A. 1991, ApJ, 374, 344
Levan, A. J., Tanvir, N. R., Cenko, S. B., et al. 2011, Science, 333, 199
Lin, D., Carrasco, E. R., Grupe, D., et al. 2011, ApJ, 738, 52
Liu, F. K., Li, S., & Chen, X. 2009, ApJ, 706, L133
Lodato, G., King, A. R., & Pringle, J. E. 2009, MNRAS, 392, 332
Lodato, G., & Rossi, E. M. 2011, MNRAS, 410, 359
Loeb, A., & Ulmer, A. 1997, ApJ, 489, 573
Lu, W., & Bonnerot, C. 2019, arXiv e-prints, arXiv:1904.12018. https://arxiv.org/abs/1904.12018
Maccarone, T. J. 2003, A&A, 409, 697
Maccarone, T. J., & Coppi, P. S. 2003, MNRAS, 338, 189
Maccarone, T. J., Gallo, E., & Fender, R. 2003, MNRAS, 345, L19
Mattila, S., Pérez-Torres, M., Efstathiou, A., et al. 2018, Science, 361, 482
McClintock, J. E., Narayan, R., & Steiner, J. F. 2014, Space Sci. Rev., 183, 295
Merloni, A., & Fabian, A. C. 2001, MNRAS, 321, 549
Merloni, A., Heinz, S., & di Matteo, T. 2003, MNRAS, 345, 1057
Merritt, D., Alexander, T., Mikkola, S., & Will, C. M. 2010, Phys. Rev. D, 81, 062002
Metzger, B. D., & Stone, N. C. 2016, MNRAS, 461, 948
Miller, M. C. 2015, ApJ, 805, 83
Nealon, R., Price, D. J., Bonnerot, C., & Lodato, G. 2018, MNRAS, 474, 1737
Parfrey, K., Giannios, D., & Beloborodov, A. M. 2015, MNRAS, 446, L61
Piran, T., Svirski, G., Krolik, J., Cheng, R. M., & Shiokawa, H. 2015, ApJ, 806, 164
Predehl, P., & Schmitt, J. H. M. M. 1995, A&A, 293, 889
Rees, M. J. 1988, Nature, 333, 523
Roth, N., Kasen, D., Guillochon, J., & Ramirez-Ruiz, E. 2016, ApJ, 827, 3
Rots, A. H., & Budavári, T. 2011, ApJS, 192, 8
Saxton, C. J., Perets, H. B., & Baskin, A. 2018, MNRAS, 474, 3307
Saxton, R. D., Read, A. M., Esquej, P., et al. 2012, A&A, 541, A106
Saxton, R. D., Read, A. M., Komossa, S., et al. 2017a, A&A, 598, A29
—. 2017b, A&A, 598, A29
Sądowski, A. 2016, MNRAS, 459, 4397
Schlafly, E. F., & Finkbeiner, D. P. 2011, ApJ, 737, 103
Shankar, F., Weinberg, D. H., & Miralda-Escudé, J. 2009, ApJ, 690, 20
Shen, R.-F., & Matzner, C. D. 2014, ApJ, 784, 87
Shiokawa, H., Krolik, J. H., Cheng, R. M., Piran, T., & Noble, S. C. 2015, ApJ, 804, 85
Stone, N., & Loeb, A. 2011, MNRAS, 412, 75
—. 2012, Physical Review Letters, 108, 061302
Stone, N., Sari, R., & Loeb, A. 2013, MNRAS, 435, 1809
Stone, N. C., & Metzger, B. D. 2016, MNRAS, 455, 859
Strubbe, L. E., & Quataert, E. 2009, MNRAS, 400, 2070
Tchekhovskoy, A., Metzger, B. D., Giannios, D., & Kelley, L. Z. 2014, MNRAS, 437, 2744
Ulmer, A. 1999, ApJ, 514, 180
van Velzen, S., Frail, D. A., Körding, E., & Falcke, H. 2013, A&A, 552, A5
van Velzen, S., Körding, E., & Falcke, H. 2011a, MNRAS, 417, L51
van Velzen, S., Stone, N. C., Metzger, B. D., et al. 2018, arXiv e-prints. https://arxiv.org/abs/1809.00003
van Velzen, S., Farrar, G. R., Gezari, S., et al. 2011b, ApJ, 741, 73
van Velzen, S., Gezari, S., Cenko, S. B., et al. 2019, ApJ, 872, 198
Wevers, T., Stone, N. C., van Velzen, S., et al. 2019a, arXiv e-prints. https://arxiv.org/abs/1902.04077
Wevers, T., van Velzen, S., Jonker, P. G., et al. 2017, MNRAS, 471, 1694
Wevers, T., Pasham, D. R., van Velzen, S., et al. 2019b, arXiv e-prints, arXiv:1903.12203. https://arxiv.org/abs/1903.12203
—. 2019c, arXiv e-prints, arXiv:1903.12203. https://arxiv.org/abs/1903.12203
Woo, J.-H., & Urry, C. M. 2002, ApJ, 579, 530
Yuan, W., Zhang, C., Feng, H., et al. 2015, arXiv e-prints. https://arxiv.org/abs/1506.07735